Impact of AGN and nuclear star formation on the ISM turbulence of galaxies: Insights from JWST/MIRI spectroscopy

Rogemar A. Riffel[1,2], Luis Colina[1], José Henrique Costa-Souza[2,1], Vincenzo Mainieri[3], Miguel Pereira Santaella[4], Oli L. Dors[5], Ismael García-Bernete[6], Almudena Alonso-Herrero[6], Anelise Audibert[7,8], Enrica Bellocchi[9,10], Andrew J. Bunker[11], Steph Campbell[12], Françoise Combes[13,14], Richard I. Davies[15], Tanio Díaz-Santos[16,17], Fergus R. Donnan[18], Federico Esposito[19], Santiago García-Burillo[19], Begoña García-Lorenzo[7,8], Omaira González Martín[20], Houda Haidar[12], Erin K. S. Hicks[21,22,23], Sebastian F. Hoenig[24], Masatoshi Imanishi[25,26], Alvaro Labiano[27], Enrique Lopez-Rodriguez[28,29], Christopher Packham[23], Cristina Ramos Almeida[7,8], Dimitra Rigopoulou[30,31], David Rosario[12], Gabriel Luan Souza-Oliveira[2,1], Montserrat Villar Martín[1], Oscar Veenema[30], and Lulu Zhang[23]

(Affiliations can be found after the references)

November 3, 2025

ABSTRACT

Active galactic nuclei (AGN), star formation (SF), and galaxy interactions can drive turbulence in the gas of the inter-stellar medium (ISM), which in turn plays a role in the SF within galaxies. The impact on molecular gas is of particular importance, as it serves as the primary fuel for SF. Our goal is to investigate the origin of turbulence and the emission of molecular gas, as well as low- and intermediate-ionization gas, in the inner few kpc of both AGN hosts and star-forming galaxies (SFGs). We use archival JWST MIRI/MRS observations of a sample consisting of 54 galaxies at $z < 0.1$. Flux measurements for the H_2 S(5)$\lambda6.9091\mu m$, [Ar II]$\lambda6.9853\mu m$, [Fe II]$\lambda5.3403\mu m$ and [Ar III]$\lambda8.9914\mu m$ emission lines along with velocity dispersion estimated by the W_{80} parameter are presented. For galaxies with coronal line emission, we include measurements for the [Mg v]$\lambda5.6098\mu m$ line. Line ratios are compared to photoionization and shock models to explore the origin of the gas emission. AGN exhibit broader emission lines than SFGs, with the largest velocity dispersions observed in radio-strong (RS) AGN. H_2 gas is less turbulent compared to ionized gas, while coronal gas presents higher velocity dispersions. The W_{80} values for the ionized gas exhibits a decrease from the nucleus out to radii of approximately 0.5–1 kpc, followed by an outward increase up to 2–3 kpc. In contrast, the H_2 line widths generally display increasing profiles with distance from the center. Correlations between the W_{80} parameter and line ratios such as H_2 S(5)/[Ar II] and [Fe II]/[Ar II] indicate that the most turbulent gas is associated with shocks, enhancing H_2 and [Fe II] emissions. Based on the observed line ratios and velocity dispersions, the [Fe II] emission is consistent with predictions of fast shock models, while the H_2 emission is likely associated with molecules formed in the post-shock region. We speculate that these shocked gas regions are produced by AGN outflows and jet-cloud interactions in AGN-dominated sources, while in SFGs, they may be created by stellar winds and mergers. This shock-induced gas heating may be an important mechanism of AGN (or stellar) feedback, preventing the gas from cooling and forming new stars.

Key words. galaxies: active – galaxies: ULIRGs – galaxies: ISM – galaxies: kinematics and dynamics

1. Introduction

The interplay between Active Galactic Nuclei (AGN) or stellar-driven galactic winds and star formation (SF) in galaxies is a crucial aspect of galaxy evolution. Both AGN and stellar winds can significantly suppress or regulate SF by injecting large amounts of energy into the interstellar medium (ISM; e.g. Silk & Rees 1998; Di Matteo et al. 2005; Hopkins et al. 2012; Dalla Vecchia & Schaye 2012; Heckman & Best 2014; Fierlinger et al. 2016; Harrison 2017; Harrison & Ramos Almeida 2024; Veilleux et al. 2020; Silk et al. 2024). The strong radiation field from AGN or nuclear starburst, nuclear winds, and jets can all generate turbulence in the gas and induce shocks, which, in turn, can disrupt the dense gas necessary for SF. These dynamic processes hinder or even prevent SF (i.e., negative feedback), as they inhibit the gas from condensing and cooling effectively. However, these mechanisms can also promote SF (i.e., positive feedback). For instance, fast outflows may enhance SF by compressing molecular clouds under pressure or by fostering SF within the outflowing material itself (Silk 2013; Zubovas & King 2014; Cresci et al. 2015; Maiolino et al. 2017; Gallagher et al. 2019; García-Bernete et al. 2021; Bessiere & Ramos Almeida 2022; Hermosa

Muñoz et al. 2024). Consequently, the balance between these outflows and the gas available for SF can have a profound impact on the star-forming potential of galaxies. A central problem is therefore to understand the origin of the gas turbulence observed in the central regions of galaxies and to establish the role of shocks in driving it. Determining whether turbulence is primarily induced by AGN outflows, radio jets, or stellar feedback, and how it regulates the physical state of the ISM, is essential to assess its impact on galaxy evolution. Addressing this issue is crucial for disentangling the mechanisms of feedback that suppress or promote star formation in different environments.

Shock-induced turbulence, triggered by AGN activity or stellar winds, can excite a variety of transitions in molecular and ionized gas, enhancing its emission across multiple wavelengths (e.g. Dopita & Sutherland 1995; Contini & Viegas 2001; Allen et al. 2008; Dors et al. 2021; Riffel et al. 2021b; Venturi et al. 2021; Appleton et al. 2017, 2023; Audibert et al. 2023, 2025; Schönell et al. 2025; Rodríguez-Ardila & Cerqueira-Campos 2025). Understanding gas emission mechanisms and the resulting turbulence in the central regions of galaxies is crucial for advancing our knowledge of how feedback processes, driven

by both stellar activity and AGN, contribute to the evolution of galaxies.

Observations of the ionized gas kinematics using integral field spectroscopy (IFS) show that AGN exhibit higher [O III]$\lambda5007$ emission line widths compared to star-forming galaxies (SFGs), extending up to distances greater than one effective radius (R_e) from the nucleus, and that high-luminosity AGN, with $L_{\text{[O III]}} > 2 \times 10^{40}$ erg s^{-1}, display a sharp increase in line widths within $0.4\,R_e$, which is associated with AGN-driven outflows (Wylezalek et al. 2020; Deconto-Machado et al. 2022; Gatto et al. 2024). Evidence of increased turbulence is detected in luminous and ultra-luminous infrared galaxies (U/LIRGs) using optical emission lines (e.g. Bellocchi et al. 2013; Arribas et al. 2014; Perna et al. 2022). Albán et al. (2024) found that radio-selected AGN exhibit broader [O III]$\lambda5007$ lines compared to those selected by other techniques, such as optical or infrared (IR) diagnostics. The authors conclude that this difference arises because radio-selected AGN represent a population in which AGN-driven kinematic perturbations have been active for longer durations, consistent with the radio emission being driven by shocks from outflows. Studies of the ionized gas in the inner kpc of AGN hosts show that broadened or complex emission line profiles are generally associated with outflows or turbulence induced by the interaction of radio jets or outflows with the ISM (e.g. Mullaney et al. 2013; Fischer et al. 2018; Freitas et al. 2018; Förster Schreiber et al. 2019; Avery et al. 2021; Kakkad et al. 2022; Zhang et al. 2024; Davies et al. 2024; Speranza et al. 2024; Esposito et al. 2024; García-Bernete et al. 2024b; Hermosa Muñoz et al. 2024). In some cases, this interaction results in additional emission from gas excited by shocks (e.g. Riffel et al. 2021b; Venturi et al. 2021).

Vibrational and ro-vibrational H$_2$ emission in the central few kpc of nearby AGN hosts and ULIRGs can be strongly enhanced by shocks from outflows or jet–cloud interactions (e.g., Ogle et al. 2010, 2025; Hill & Zakamska 2014; Colina et al. 2015; Kristensen et al. 2023; Riffel et al. 2021a,c, 2025; Costa-Souza et al. 2024; Villar Martín et al. 2023; Leftley et al. 2024; Bohn et al. 2024; Dasyra et al. 2024). These shocks can heat the gas, promoting the excitation of H$_2$ molecules and leading to the emission of these diagnostic lines. A comparison of the emission lines from hot molecular gas and ionized gas, using near-IR lines, shows that the former are typically narrower than the latter, but both are observed in kinematically disturbed regions (KDRs) around AGN and in ULIRGs (e.g. Emonts et al. 2017; Ramos Almeida et al. 2017, 2019, 2025; Bianchin et al. 2022; Riffel et al. 2023; Zanchettin et al. 2025).

With the use of the James Webb Space Telescope (JWST; Gardner et al. 2023) Mid-Infrared Instrument medium-resolution spectrometer (MIRI/MRS; Wright et al. 2015, 2023), it is possible to map the kinematics of multiple gas phases in the central regions of galaxies, including areas that are heavily obscured at optical wavelengths, as the extinction in the mid-IR is up to $\sim$40 times lower than in the optical (Gordon et al. 2023). This allows unprecedented access to the deeply embedded gas emission structures and processes in dusty galactic nuclei, such as AGN-driven winds, turbulence in the ISM produced by outflows and jets, and circumnuclear SF. Here, we use archival JWST MIRI/MRS observations of a large sample of AGN hosts and ULIRGs at redshifts $z < 0.1$ to compare the kinematics across warm molecular gas and low- to moderate-ionization phases, and investigate the origin of the gas emission and turbulence in these galaxies. We focus on the H$_2$ $0-0$ S(5)$\lambda6.9091\mu$m transition and a set of low- and medium-ionization fine-structure lines, including [Ar II]$\lambda6.99\,\mu$m, [Fe II]$\lambda5.34\,\mu$m, and [Ar III]$\lambda8.99\,\mu$m. These

lines are among the brightest in the mid-IR spectra, and they often trace spatially extended emission in nearby AGN and SFGs. Their excitation can arise from different mechanisms, such as photoionization by massive stars or AGN, as well as shocks produced by stellar and AGN-driven outflows and jets. The analysis of both the line intensities and their kinematics therefore provides powerful diagnostics of the physical conditions and dominant excitation processes in the nuclear regions of galaxies.

This paper is organized as follows. Section 2 describes the sample, and Section 3 presents the data and measurements. Our main results are presented in Section 4, followed by a discussion on the origin of the gas emission and turbulence in Section 5. Finally, Section 6 summarizes our key conclusions.

2. The sample

Our goal is to investigate the origin of the emission and the dynamics of warm molecular gas as well as low- and medium-ionization ionized gas. In local galaxies ($z \lesssim 0.1$), the aforementioned emission lines are observed in Channels 1 and 2 of the MIRI/MRS, which provide angular resolutions of approximately 0.35–0.40 arcsec (FWHM; Law et al. 2023). Additionally, we used the [Mg V]$\lambda5.6098\,\mu$m emission line to identify objects with high-ionization gas, and H$_2$ S(3)$\lambda9.6649\,\mu$m to investigate the origin of the molecular gas emission. The ionization potentials are 7.9 eV for Fe II (Nave & Johansson 2013), 15.8 eV for Ar II (Sansonetti & Martin 2005), 27.6 eV for Ar III (Kaufman & Whaling 1996), and 109 eV for Mg V (Biémont et al. 1999), as listed in the National Institute of Standards and Technology (NIST) Atomic Spectra Database Ionization Energies Data (Kramida et al. 2014).

The sample was defined as follows: we queried the Mikulski Archive for Space Telescopes (MAST) Portal for JWST observations of galaxies with $z < 0.1$ obtained using the MIRI instrument in the MRS observing mode. The redshift threshold was selected to allow the study of gas emission and kinematics on scales of hundreds of parsecs, enabling meaningful comparisons across objects with similar spatial resolutions. Our search was limited to projects with publicly available data that provide complete spectral coverage with MIRI/MRS, including all three sub-bands (Short, Medium, and Long) and extended emission in the relevant emission lines, resulting in a sample of 54 galaxies. Table 1 summarizes the properties of the sample, including the distance (D), hard X-ray (14–195 keV) luminosity (L_{BAT}), radio powers at 1.4 GHz and 4.8 GHz ($P_{1.4\,\text{GHz}}$ and $P_{4.8\,\text{GHz}}$), H-band luminosity (L_{H}), and infrared luminosity (L_{IR}) of each galaxy.

In our sample, 25 objects (46%) are detected in the Swift BAT survey, while 51 objects (94%) have 1.4 GHz data, and 30 objects (56%) have measurements at 4.8 GHz (see notes in Table 1 for references). Table A.1 presents the list of galaxies and the corresponding details of the observational proposals. Strong correlations are found between radio power and X-ray luminosity for the objects detected in both bands. Specifically, the 1.4 GHz and 4.8 GHz radio powers show Pearson correlation coefficients of 0.79 and 0.85, respectively, with the X-ray luminosity. Additionally, for the objects detected at both radio frequencies, the 4.8 GHz and 1.4 GHz radio powers are tightly correlated, closely following a 1:1 relation, with a Pearson correlation coefficient of 0.96.

In this work, we are not focused on discussing individual objects, many of which exhibit a rich abundance of physical properties. Instead, our goal is to investigate the general properties of the sample, specifically the physical characteristics of

Table 1. Properties of the sample.

(1) Object	(2) D [Mpc]	(3) $\log L_{\mathrm{BAT}}$ [erg/s]	(4) $\log P_{1.4\mathrm{GHz}}$ [W/Hz]	(5) $\log P_{4.8\mathrm{GHz}}$ [W/Hz]	(6) $\log L_{\mathrm{H}}$ [erg/s]	(7) $\log L_{\mathrm{IR}}$ [erg/s]	(8) Subsamples
Arp220	78.8	–	23.36	23.20	43.19	45.68	SF
Centaurus A	3.1[a]	42.19	21.71[a]	21.83[a]	41.19	43.25	BAT; [Mg V]
Cygnus A	240.9	44.98	26.74[b]	27.15[b]	43.58	45.79	BAT; RS; [Mg V]; IR
ESO137-G034	31.0[b]	42.43	–	–	42.54	44.05	BAT; [Mg V]
ESO420-G13	51.0	–	22.30	–	43.06	44.95	[Mg V]; IR
IC5063	48.6	43.28	23.73[c]	23.17[c]	43.06	45.13	BAT; RS; [Mg V]; IR
IIZw96	154.7	–	23.08	22.26[d]	42.72	45.82	IR
IRAS05189-2524	188.8	43.60	23.07	–	44.13	46.13	BAT; IR
IRAS07251-0248	375.2	–	23.27	–	43.73	45.91	IR
IRAS09022-3615	255.6	–	23.80	–	43.77	45.92	RS; IR
IRAS09111-1007	232.0	–	22.26	–	43.81	45.38	SF
IRAS10565+2448	184.7	–	23.35	–	43.91	45.68	SF
IRAS13120-5453	131.8	–	23.49[c]	23.12[c]	43.96	45.91	SF
IRAS14348-1447	352.8	–	23.69	–	43.74	45.00	SF
IRAS15250+3609	236.6	–	22.96	–	43.56	45.89	IR
IRAS19297-0406	367.4	–	23.64	–	43.89	45.85	SF
IRAS19542+1110	278.4	–	23.25	–	43.97	45.72	SF
IRAS20551-4250	184.3	–	23.08[e]	–	43.58	45.85	IR
IRAS22491-1808	333.2	–	22.86	–	43.61	45.78	SF
IRAS23128-5919	191.1	–	–	–	43.31	45.85	IR
IRASF01364-1042	206.7	–	22.87	22.76	43.26	45.20	IR
IRASF08572+3915NW	249.4	–	22.48	–	43.09	46.07	IR
IRASF14378-3651	289.9	–	23.50	–	43.71	45.68	IR
IRASF23365+3604	276.3	–	23.37	–	43.78	45.81	IR
M81	3.3[c]	40.42	20.05	20.11	41.80	42.32	BAT
M87	15.8[d]	–	24.64	24.24	42.23	42.79	RS
M94	4.2[e]	–	19.41	20.35	42.09	42.84	SF
M104	8.0[f]	–	20.86	21.08[f]	42.43	42.37	SF
MCG-05-23-016	36.6	43.52	21.36	–	42.97	44.70	BAT; [Mg V]; IR
Mrk231	180.7	–	24.06	24.19	44.81	46.46	RS; IR
Mrk273	160.0	43.18	23.63	23.33	43.73	45.81	BAT; [Mg V]; IR
NGC0253	3.5[e]	–	21.59	21.55[h]	41.38	44.37	SF
NGC0424	50.4	42.81	21.84	–	43.23	44.86	BAT; IR
NGC1052	19.2[g]	42.14	22.60	23.14[f]	42.75	43.63	BAT
NGC1068	10.1[h]	41.66	22.77	22.29[g]	42.90	45.23	BAT; [Mg V]; IR
NGC1365	18.3[i]	42.40	22.18	22.08[h]	42.00	44.90	BAT; [Mg V]
NGC1566	6.6[g]	41.01	20.93[c]	20.72[i]	41.62	42.71	BAT; [Mg V]
NGC1808	9.5[j]	–	21.76	21.41[i]	42.21	44.47	SF
NGC3081	23.8[k]	42.74	20.56	–	42.30	44.10	BAT; [Mg V]
NGC3256N	40.1	–	–	–	43.06	45.60	SF
NGC3256S	40.1	–	23.07[c]	22.78[i]	43.17	–	IR
NGC4258	6.8[l]	41.11	21.44	21.23[b]	41.80	42.76	BAT
NGC4395	4.4[m]	40.81	19.75	18.07[i]	39.78	41.61	BAT; [Mg V]
NGC5506	23.8[n]	43.21	22.36	22.09[k]	42.92	44.57	BAT; [Mg V]; IR
NGC5728	39.0[o]	43.18	22.10	–	42.86	44.36	BAT; [Mg V]
NGC6240	104.2	43.94	23.73	23.32	43.89	45.66	BAT, RS; [Mg V]
NGC6552	113.7	43.50	22.68	22.70[d]	43.48	45.25	BAT; [Mg V]; IR
NGC7172	37.4	43.42	21.79	–	42.88	44.20	BAT; [Mg V]; IR
NGC7319	96.5	43.60	22.76	–	43.11	44.59	BAT; [Mg V]; IR
NGC7469	69.7	43.61	23.01	22.60	43.75	45.56	BAT; [Mg V]
NGC7582	23.2	42.72	22.22[e]	21.68[k]	43.02	44.77	BAT; [Mg V]; IR
UGC05101	168.7	43.37	23.75	23.40	43.88	45.54	BAT, RS; IR
VV114	86.0	–	23.33	22.92[f]	43.20	45.58	IR
VV340a	144.3	–	23.34	22.81	43.87	45.05	[Mg V]

Notes. (1) Galaxy name; (2) Distances were taken from the literature when available; otherwise, they were estimated from the redshift, assuming a cosmology with $h = 0.7$, $\Omega_m = 0.3$, and $\Omega_\Lambda = 0.7$. Superscript letters indicate the corresponding references: a: Majaess et al. (2008), b: Willick et al. (1997), c: Gerke et al. (2011), d: Oldham & Auger (2016), e: Radburn-Smith et al. (2011), f: Spitler et al. (2006), g: Tully et al. (2013), h: Nasonova et al. (2011), i: Riess et al. (2016), j: Tully et al. (2016), k: Bottinelli et al. (1984), l: Hoffmann & Macri (2015), m: Sabbi et al. (2018), n: Karachentsev et al. (2014), o: Rest et al. (2014); (3) Hard X-ray (14-195 keV) luminosity from Oh et al. (2018); (4) 1.4 GHz power taken from the NRAO VLA Sky Survey (NVSS; Condon et al. 1998), and supplemented with additional data from the literature (indicated by superscripts): a: Tingay et al. (2003), b: Steenbrugge et al. (2010), c: Allison et al. (2014), d: Brown et al. (2017), e: Condon et al. (1996); (5) 4.8 GHz radio power taken from the Green Bank 4.85 GHz survey (Gregory et al. 1996), with additional data from the literature (indicated by superscripts): a: Tingay et al. (2003), b: Becker et al. (1991), c: Wright et al. (1994), d: Gregory & Condon (1991), e: Baan & Klöckner (2006), f: Griffith et al. (1994), g: Sajina et al. (2011), h: Stil et al. (2009), i: Wright et al. (1994), j: Nagar et al. (2005), k: Orienti & Prieto (2010). (6) H-band luminosity from The Two Micron All Sky Survey (2MASS; Skrutskie et al. 2006); (7) IR luminosity obtained from the WISE W4 luminosity (Wright et al. 2010) using the relation from Cluver et al. (2017). The northern nucleus of NGC 3256 is an order of magnitude brighter in IR than the southern nucleus (Bohn et al. 2024); thus, we quote L_{IR} only for the northern nucleus. High-resolution IR data reveal an AGN in the southern nucleus (Ohyama et al. 2015), which is included in our IR AGN sample. For IRAS 13120-5453, L_{IR} was estimated from the 25μm IRAS flux, as WISE magnitudes are unavailable; (8) The subsamples to which each object belongs.

Table 2. Mean properties for each subsample. Uncertainties are the standard deviation of each parameter.

Subsample	BAT AGN	RS AGN	[Mg v] AGN	IR AGN	SF
# of galaxies	25	7	21	27	13
$\langle \log D/\mathrm{Mpc} \rangle$	1.50 ± 0.56	2.03 ± 0.44	1.55 ± 0.51	2.02 ± 0.41	1.80 ± 0.78
$\langle \log L_{\mathrm{H}}/\mathrm{erg\ s^{-1}} \rangle$	42.79 ± 0.98	43.60 ± 0.80	42.81 ± 0.97	43.39 ± 0.47	43.17 ± 0.87
$\langle \log L_{\mathrm{IR}}/\mathrm{erg\ s^{-1}} \rangle$	44.46 ± 1.18	45.33 ± 1.19	44.58 ± 1.04	45.45 ± 0.57	44.97 ± 1.17
$\langle \log P_{1.4}/\mathrm{W\ Hz^{-1}} \rangle$	22.23 ± 1.65	24.35 ± 1.11	22.42 ± 1.60	23.07 ± 1.00	22.51 ± 1.29

warm molecular gas and low- to moderate-ionization gas. Consequently, we do not present individual maps for all galaxies. We present our results by dividing the sample into five subsamples, where a single galaxy may belong to more than one group, defined as follows:

- BAT AGN: This subsample of X-ray selected AGN is composed of 25 galaxies. It is obtained by cross-matching the sample with the 105-month catalog of hard X-ray sources (14–195 keV) from the Swift Burst Alert Telescope (BAT) survey (Oh et al. 2018), including all X-ray detected sources. The hard X-ray emission offers a direct measurement of AGN activity, as it predominantly captures the intrinsic emission from the AGN rather than scattered or reprocessed emissions. Additionally, it is significantly less affected by line-of-sight obscuration compared to optical wavelengths or softer X-ray bands.

- RS AGN: This subsample of radio-strong (RS) AGN is composed of 7 galaxies. SFGs typically exhibit 1.4 GHz radio luminosities below $P_{1.4\mathrm{GHz}} = 10^{23}$ W Hz^{-1}, although some can reach up to $\sim 10^{24}$ W Hz^{-1} (Condon et al. 2002; Jose et al. 2024). AGN, on average, exhibit radio luminosities higher than those expected purely from SFGs (e.g. Condon et al. 2002), due to additional emission from jets (Padovani 2017) and/or shocks generated by outflows (Zakamska et al. 2016). The standard definition of radio-loud AGN identifies them as those with a ratio of 5 GHz radio luminosity to B-band luminosity of $L_{5\mathrm{GHz}}/L_{\mathrm{B}} \gtrsim 10$ (e.g. Kellermann et al. 1989). However, several studies use the 1.4 GHz radio power to distinguish between radio-loud and radio-quiet AGN, often defining thresholds at $P_{1.4\mathrm{GHz}} = 10^{23}$ W Hz^{-1} (e.g. Best et al. 2005) or $P_{1.4\mathrm{GHz}} = 10^{24}$ W Hz^{-1} (e.g. Tadhunter 2016). Since most galaxies in our sample are detected at 1.4 GHz, we use their observed radio powers to define a subsample of RS AGN. Only three objects in our sample have $\log P_{1.4\,\mathrm{GHz}}/[\mathrm{W\ Hz^{-1}}] > 24$. On the other hand, our sample includes ULIRGs, for which the commonly used threshold of $\log P_{1.4\,\mathrm{GHz}}/[\mathrm{W\ Hz^{-1}}] > 23$ may be insufficient to ensure the presence of an AGN. Therefore, we adopt an intermediate value of $\log P_{1.4\,\mathrm{GHz}}/[\mathrm{W\ Hz^{-1}}] > 23.7$, which lies between the thresholds commonly used in the literature. This sample includes four ULIRGs (i.e. IRAS 09022−3615, Mrk 231, NGC 6240, and UGC 05101) all of which are classified as AGN using the other methods adopted in this work. In these objects, a significant fraction of the radio emission may still be attributed to SF. Among all the RS AGN, the only galaxy not included in any other AGN sample is the radio galaxy M 87. In addition, we note that only two galaxies in this sample exhibit a clear radio excess: Cygnus A and M 87. This is evidenced by $q_{23} < 0$, where $q_{23} = \log(S_{23\mu m}/S_{1.4\mathrm{GHz}})$, with $S_{23\mu m}$ and $S_{1.4\mathrm{GHz}}$ representing the flux densities at 23 μm and 1.4 GHz, respectively (Radcliffe et al. 2021). Therefore, interpretations regarding the role of AGN in this subsample should be approached with caution.

- [Mg v] AGN: This subsample is composed of 21 galaxies with coronal line emission. Coronal lines are emitted by highly ionized gas with ionization potentials IP$\gtrsim$100 eV. They serve as reliable indicators of AGN activity, generated either by photoionization from the AGN's intense radiation field or by shocks associated with jets and outflows (e.g. Rodríguez-Ardila & Cerqueira-Campos 2025; Ramos Almeida et al. 2025). We use the [Mg v]$\lambda 5.6098\mu$m emission line to select galaxies for this subsample, using the MIRI MRS datacubes. We show the [Mg v] flux maps and line profiles for each galaxy in Fig. B.1.

- IR AGN: This subsample is composed of 27 IR selected galaxies. AGN exhibit an excess of IR emission, which arises from the dusty torus heated by the radiation from the central engine (Antonucci 1993; Netzer 2015). We select the IR AGN sample based on magnitudes from the Wide-field Infrared Survey Explorer (WISE; Wright et al. 2010). We adopt the definition of Stern et al. (2012), considering AGN as objects with a color criterion of $W1 - W2 \geq 0.8$. This criterion efficiently identifies AGN even in galaxies with significant host galaxy contamination and is particularly sensitive to dust-obscured AGN populations (Assef et al. 2010; Stern et al. 2012).

- SF: The subsample comprises 13 SFGs that are not classified as AGN by any of the methods described above, and is predominantly composed of U/LIRGs (7 ULIRGs and 2 LIRGs). Although some of these galaxies show evidence of buried or obscured AGN, their gas excitation is predominantly driven by SF (Cicone et al. 2014; Su et al. 2023; García-Bernete et al. 2025).

Table 2 presents the mean properties of each subsample. The H-band luminosity can be used as a reliable proxy for stellar mass (Davies et al. 2015), allowing us to compare the stellar mass distributions across different subsamples. The sample includes objects with L_{H} in the range 10^6-10^{11} L$_\odot$. The mean H-band luminosities for all subsamples are similar, with the BAT AGN and [Mr v] AGN subsamples presenting slightly smaller values than the other samples. In addition, we performed two-sample Kolmogorov–Smirnov (KS) tests to assess whether the H-band luminosity distributions of the AGN and SF samples differ significantly. The p-values indicate that the AGN and SF samples are drawn from the same parent population.

The four AGN subsamples were defined using tracers of different physical processes. The BAT subsample directly probes the emission of the hot corona located above the AGN accretion disk, while the RS subsample is associated with the mechanical energy released in the form of jets. The [Mg v] subsample is related to the local gas physics, as it primarily traces the ionization parameter rather than directly probing the AGN emission, similar to optical diagnostic diagrams (Baldwin et al. 1981; Negus et al. 2023). Coronal line emission, however, can also be associated with shocked gas regions in the inner $\sim$1 kpc of AGN hosts (Rodríguez-Ardila & Cerqueira-Campos 2025; Rodríguez-Ardila et al. 2025). Finally, the IR subsample traces the physics of the hot dust heated by AGN radiation. Since these physical processes are interconnected and can occur simultaneously in an

AGN, many of our objects appear in more than one subsample. Fig. 1 shows the Venn diagram illustrating the overlap among the different AGN subsamples.
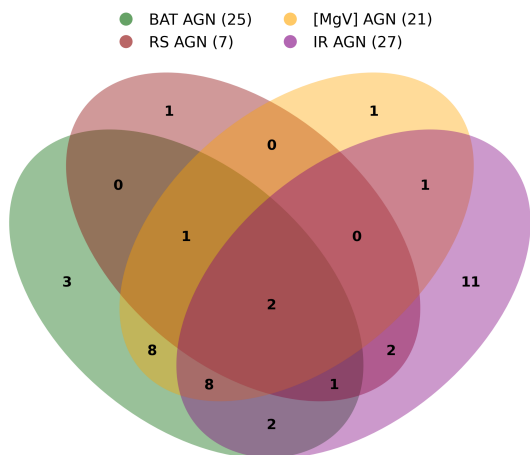

Fig. 1. Venn diagram illustrating the overlap among the different AGN subsamples.
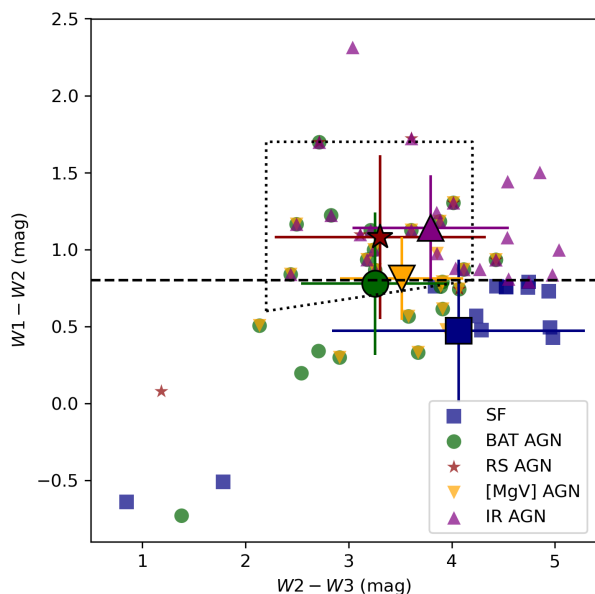

Fig. 2. WISE color–color diagram showing the five subsamples, as indicated by the symbols. The uncertainties are comparable to the symbol sizes. The large symbols with error bars correspond to the mean values for each subsample, with the error bars representing the standard deviation. The dashed line represents the threshold $W1 - W2 = 0.8$, while the dotted polygon marks the region typically occupied by Seyfert galaxies (Jarrett et al. 2011).

In Fig. 2 we present the WISE color-color diagram for our subsamples. The mean $W1-W2$ and $W2-W3$ values for all AGN subsamples fall within the region typically occupied by Seyfert galaxies, as indicated by the dotted polygon. The IR AGN subsample includes representatives of dustier objects, exhibiting larger colors along both axes of the diagram; some BAT and [Mg v] AGN show lower $W1 - W2$ values than typical Seyfert

galaxies, consistent with low-luminosity AGN; and objects in the SF sample are located in a region consistent with Starburst galaxies; all three associations are consistent with the locations of these classes among WISE objects (Wright et al. 2010).

3. Data Reduction and Measurements

We use archival mid-IR JWST spectroscopic data obtained with the MIRI/MRS instrument (Wells et al. 2015; Labiano et al. 2021; Argyriou et al. 2023) of a sample of nearby galaxies. The observations were carried out using different observational strategies, according to the scientific objectives of the approved proposals. We downloaded the processed data from MAST archive, using the following filters: obs_collection='JWST', intentType='science', dataRights='PUBLIC', instrument_name='MIRI/IFU', calib_level=3, proposal_id=pid, obs_id='jw*{pid}-c*', where pid refers to the proposal IDs listed in the table, identified from the list of approved projects up to cycle 3. These data were processed using version 1.16.1 of the JWST Science Calibration Pipeline (Bushouse et al. 2024), employing the reference file jwst_1303.pmap.

The MIRI/MRS field of view (FoV) for channel 1 is 3.2×3.7 arcsec^2, while channel 2 has a FoV of 4.0×4.8 arcsec^2. Before performing the emission line flux and kinematic measurements, we rebinned the channel 1 data cubes to a spaxel size of 0.17 arcsec and convolved them with a Gaussian function with FWHM = 0.40 arcsec, in order to match the angular sampling and spatial resolution of the channel 2 cubes. Subsequently, each spaxel in the cube was replaced with the average of its nearest neighbors within a 3×3 spaxel box. This process minimizes residual instrumental effects, particularly the continuum wiggles caused by the undersampling of the point spread function (PSF; Law et al. 2023).

We performed the flux measurements and calculated the velocity dispersion, parametrized by the W_{80} parameter, which is defined as the width encompassing 80 per cent of the total line flux. These measurements were carried out for the following emission lines: H$_2$ S(5)λ6.9091μm, H$_2$ S(3)λ9.6649μm, [Ar II]λ6.9853μm, and [Ar III]λ8.9914μm, [Fe II]λ5.3403μm and [Mg v]λ5.6098μm. For each emission line, we subtracted the continuum contribution by fitting a linear function to regions adjacent to the line. The line profile was then integrated within a 3000 km s^{-1} window centered on the emission line. We only considered spaxels where the emission line was detected with a signal-to-noise ratio $snr > 5$, determined as the ratio between the line profile amplitude and the standard deviation of the adjacent continuum within a 1000 km s^{-1} window. Fig. 3 presents examples of flux and W_{80} measurements for the emission lines H$_2$ S(5)λ6.9091μm, [Ar II]λ6.9853μm, [Fe II]λ5.3403μm, and [Ar III]λ8.9914μm in the galaxy Arp 220. The gray regions indicate areas where the corresponding emission line is either not detected with $snr > 5$ or lies outside the FoV of the MIRI instrument. The measured W_{80} values were corrected for instrumental broadening using the resolving power described by $R = 4603 - 128 \times \lambda[\mu m]$ (Jones et al. 2023), along with the relation $W_{80} = 1.09 \times$ FWHM for a Gaussian profile.

4. Results

We use the W_{80} parameter to trace the velocity dispersion of the gas, which can be associated with turbulence and kinematic disturbances in the nuclear regions. In Fig. 4, we present the nuclear
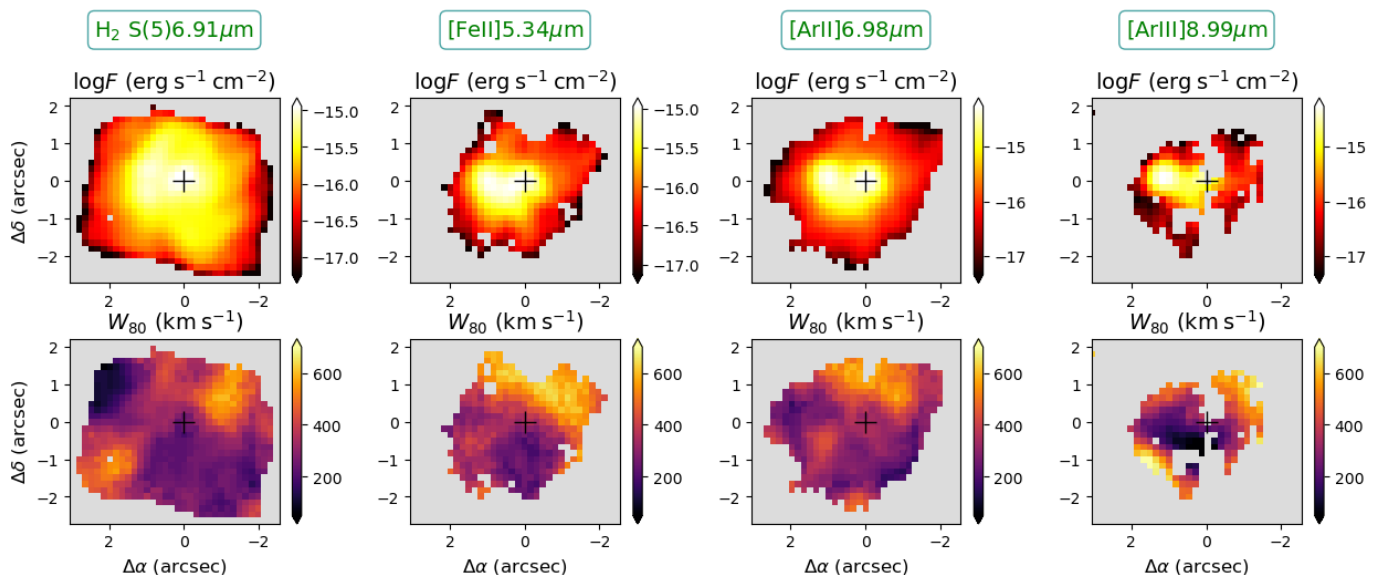
Fig. 3. Examples of flux (top panels) and W_{80} (bottom panels) maps for Arp 220. From left to right, the H$_2$ S(5)λ6.9091μm, [Ar II]λ6.9853μm, [Fe II]λ5.3403μm, and [Ar III]λ8.9914μm are shown. The central crosses identify the location of the peak of the continuum, corresponding to the western nucleus, used as reference to calculate radial distances from the galaxy nucleus. The gray regions correspond to locations where the corresponding emission line is not detected with *snr* > 5 and regions not covered by the MRS FoV.

W_{80} distributions for the H$_2$ S(5)λ6.9091μm, [Fe II]λ5.3403μm, [Ar II]λ6.9853μm, and [Ar III]λ8.9914μm emission lines (from top to bottom) for the BAT AGN, RS AGN, [Mg v] AGN, IR AGN and SF subsamples (from left to right, respectively). These values are computed as the flux-weighted mean W_{80} values measured for spaxels within a 0.5 arcsec radius aperture. We observe that, for all AGN samples, the H$_2$ emission lines consistently present the lowest mean values of W_{80}. Furthermore, the W_{80} values of the ionized gas emission lines increase from [Fe II] through [Ar II], reaching the highest values for [Ar III], following the order of increasing ionization potential. These higher W_{80} values indicate enhanced gas turbulence in the more highly ionized regions. For example, the mean difference of W_{80} between [Fe II] and H$_2$, considering all AGN subsamples, is 56 ± 28 km s^{-1}, while the mean difference between [Ar III] and [Fe II] is 115 ± 35 km s^{-1}. On the other hand, the SF subsample shows similar mean W_{80} values for H$_2$, [Fe II], and [Ar II], while [Ar III] exhibits higher values. Finally, it is noted that the AGN samples include objects with $W_{80} > 500$ km s^{-1}, which exceed the values expected for motions solely governed by the gravitational potential of galaxies and are commonly used as a criterion to identify outflows in AGN hosts in the local universe (e.g. Wylezalek et al. 2020). Even smaller values, around $\gtrsim 300$ km s^{-1}, have also been linked to ionized gas outflows in low-luminosity AGN (Riffel et al. 2023; Gatto et al. 2024). Such high W_{80} also reflects strong turbulence associated with AGN-driven outflows. In addition, three galaxies in the SF sample–M 104, IRAS 19542+1110, and IRAS 13120−5453–exhibit nuclear W_{80} values exceeding 500 km s^{-1}. In M 104, this is observed across all ionized-gas emission lines, while in the other two it is present only in [Ar III].

In Fig. 5 we show W_{80} radial profiles for the H$_2$ (top left), [Fe II] (top right), [Ar II] (bottom left) and [Ar III] (bottom right) for the five subsamples. These radial profiles were constructed by computing the median W_{80} and median radii values within 250 pc radial bins, considering all spaxels in all galaxies in each sample. The radial distances are calculated relative to the position of the peak of the continuum emission at 6.75 μm. The bin size was chosen as a compromise between the angular resolu-

tion for more distant objects and the field-of-view size for nearer ones. The bin width is smaller than the PSF radius only for the four most distant objects ($D \gtrsim 300$ Mpc). The number of galaxies used in each bin is indicated next to each data point. Fig. C.1 presents the same W_{80} radial profiles, but grouping the four emission lines for each subsample.

The lowest values of W_{80} at most radii are found for the SF sample across all emission lines within distances up to 1.5–2 kpc, beyond which the number of objects with spatial coverage for larger distances becomes small. An exception is seen in [Ar III], where the W_{80} values for SFGs at distances greater than 1 kpc exceed those in AGN; however, only two SFGs show emission in this line beyond 1 kpc. For the ionized gas lines, there is a trend of decreasing W_{80} values from the nucleus up to $\sim 0.5 - 1$ kpc, followed by an increase with radius in more distant regions. These variations likely reflect changes in the turbulent motions of the gas across different spatial scales. This behaviour is less evident in [Fe II], where the radial profiles show more monotonically increasing values with the distance from the nucleus, except for the RS AGN. At distances larger than $\sim$2 kpc, the W_{80} values start to decrease, but the number of objects with measurements at these scales is very reduced. For H$_2$, the radial profiles show values increasing with distance from the nucleus for all subsamples, except in the RS AGN, where a similar behavior to that described above for the ionized gas is observed. Furthermore, the gas velocity dispersion values in our SF sample are significantly higher than those observed in low-z SFGs, which typically exhibit $\sigma \approx 10$–40 km s^{-1} or $W_{80} \approx 25$–100 km s^{-1} (e.g., Epinat et al. 2010). Instead, our measurements are comparable to those observed in local U/LIRGs, which are often attributed to gas outflows (e.g., Piqueras López et al. 2012; Bellocchi et al. 2013; Arribas et al. 2014).

Emission-line flux ratios can be used to investigate the origin of gas emission, while the line widths provide insights into the origin of gas turbulence and the behaviors observed in the radial profiles of W_{80}. Fig. 6 presents W_{80} density maps for [Fe II]λ5.3403μm versus the flux ratios H$_2$ S(5)λ6.9091μm/[Ar II]λ6.9853μm (top pan-

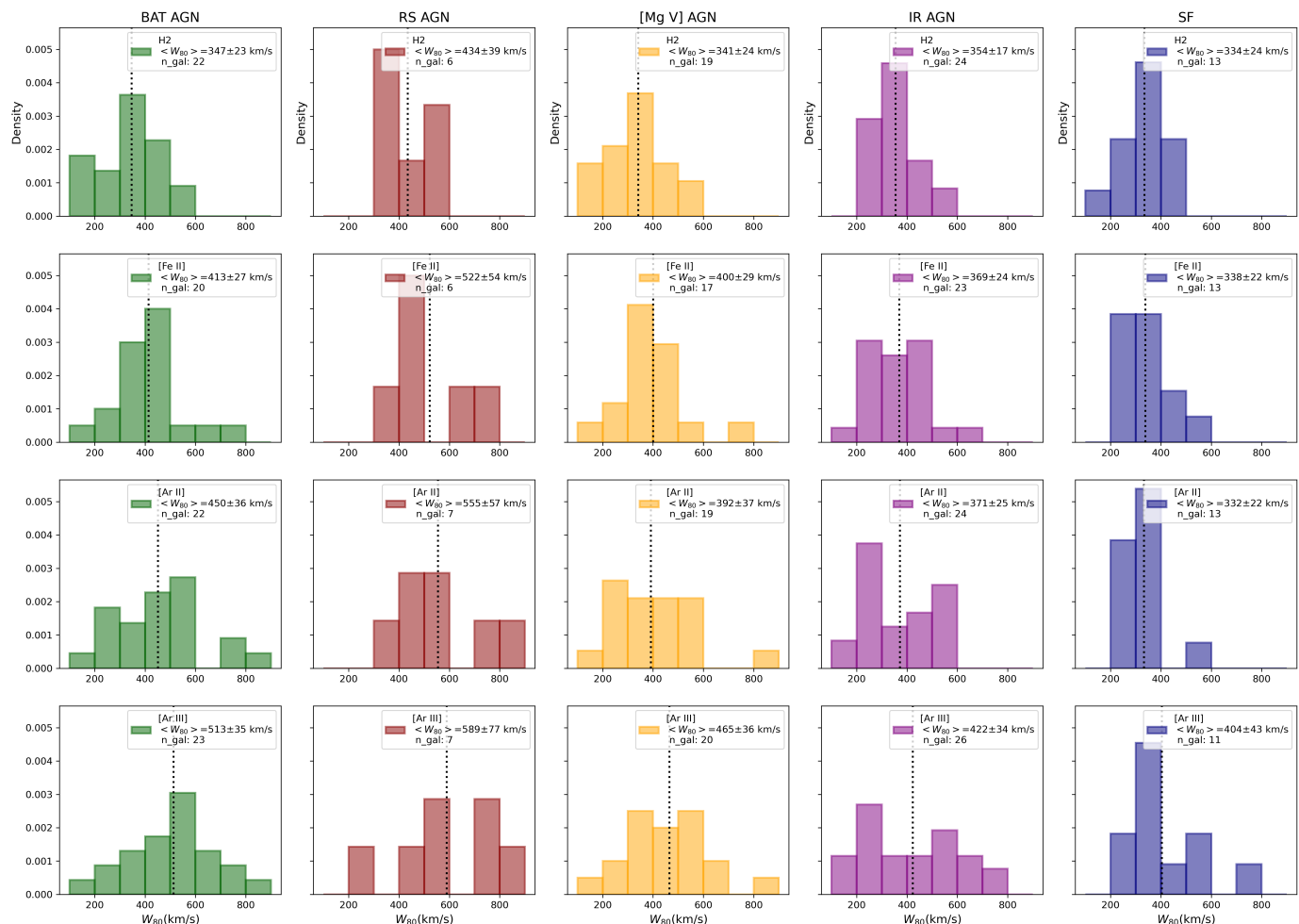**Fig. 4.** Nuclear W_{80} values for the H_2 S(5), [Fe II], [Ar II], and [Ar III] emission lines — ordered by increasing ionization potential from top to bottom — are shown for the five subsamples, displayed in separate columns. The W_{80} values are estimated as the flux weighted mean W_{80} values of spaxels within a radius of 0.5 arcsec centered at the peak or the continuum emission. The mean values (indicated by vertical dotted lines), standard error, and the number of galaxies are displayed in each panel.

els), [Fe II]$\lambda 5.3403\mu$m/[Ar II]$\lambda 6.9853\mu$m (central panels) and [Ar III]$\lambda 8.9914\mu$m/[Ar II]$\lambda 6.9853\mu$m (bottom panels) for the different subsamples. These maps were constructed using spaxel-based measurements.

As observed in Fig. 6, the SF sample exhibits the highest densities at $W_{80} \lesssim 300\,\mathrm{km\,s^{-1}}$, while the AGN samples display higher values, typically ranging between 300 and 600 $\mathrm{km\,s^{-1}}$, with a secondary clustering in the distribution of points at values similar to those of SFGs, except for the RS AGN. The clustering of points with lower values of W_{80} and line ratio (the secondary clustering) is associated with spaxels located closer to the nucleus, compared to the clustering of points with higher values of these parameters. For regions with $W_{80} < 300\,\mathrm{km\,s^{-1}}$ (and low line ratios, as seen in Fig. 6), the median distance of spaxels from the nucleus is 234, 282, and 340 pc for the BAT, [Mg V], and IR AGN samples, respectively. For regions with $W_{80} > 300\,\mathrm{km\,s^{-1}}$, these distances increase to 267, 321, and 534 pc for the same samples. The secondary clustering detected in the AGN samples is probably linked to SF within the MIRI FoV, as observed in several of these galaxies (e.g. Ricci et al. 2018; Zanchettin et al. 2024; Cassanta et al. 2025). The highest W_{80} values for the AGN samples reach 800 $\mathrm{km\,s^{-1}}$, whereas for the SF sample, the maximum values reach up to 600 $\mathrm{km\,s^{-1}}$. The BAT and [Mg V] AGN subsamples show remarkably simi-

lar distributions in these plots. This is not surprising, since both are direct tracers of AGN emission, either through the X-rays produced by the central engine or through the high-energy photons required to ionize the coronal gas. For all subsamples, a trend of increasing H_2 S(5) $\lambda 6.9091\,\mu$m/[Ar II] $\lambda 6.9853\,\mu$m and [Fe II] $\lambda 5.3403\,\mu$m/[Ar II] $\lambda 6.9853\,\mu$m with the line width of [Fe II] is observed. However, the SF sample exhibit lower values of flux ratios compared to the AGN samples. A similar trend is observed with the [Ar III]/[Ar II] flux ratio (bottom panels), a diagnostic of the ionization degree of the gas since it involves lines of the same element with different ionization states. However, this trend is only evident for the BAT, [Mg V], and IR AGN samples. For the SF sample, most points are concentrated at low flux ratios and W_{80} values, with some contours extending to higher values. In contrast, the RS AGN sample exhibits two structures: one with $W_{80} < 600\,\mathrm{km\,s^{-1}}$ spanning a wide range of [Ar III]/[Ar II] ratios, and another with $W_{80} > 600\,\mathrm{km\,s^{-1}}$ and lower flux ratios.

5. Discussion

As presented in the previous section, we found that: (i) AGN exhibit higher gas turbulence, as indicated by the emission line widths, compared to SFGs. (ii) There is a trend
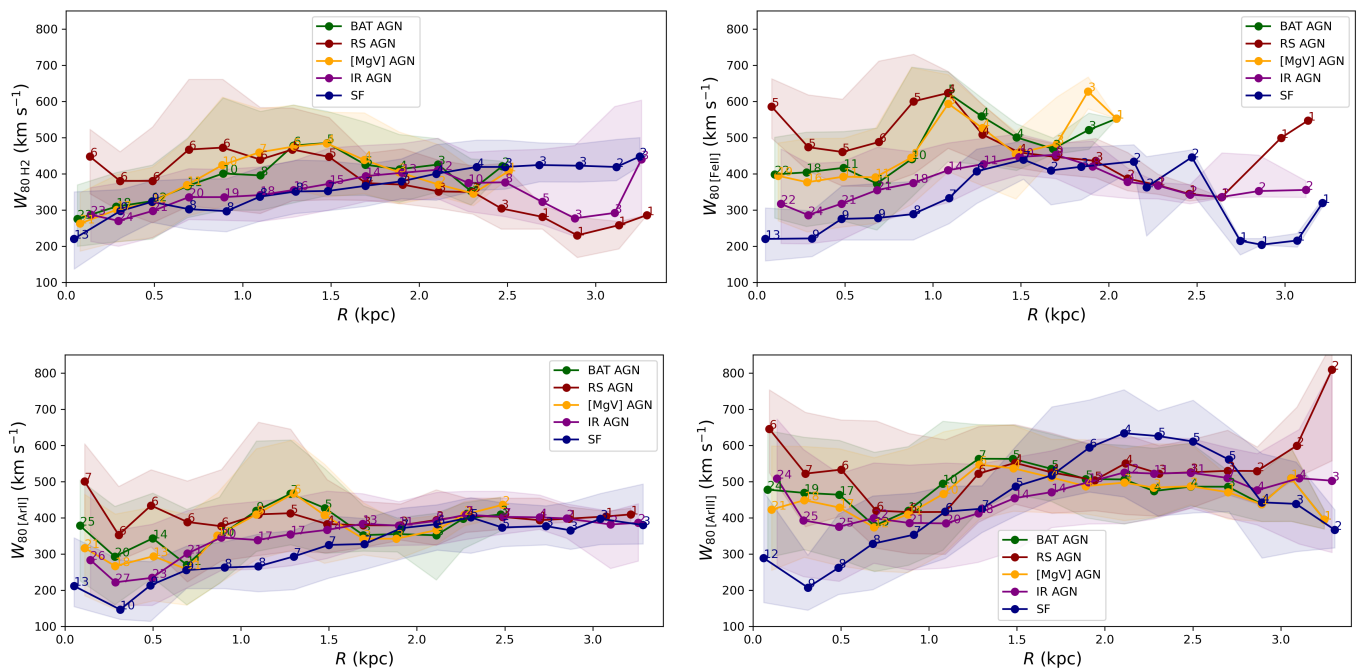
Fig. 5. Radial W_{80} profiles for H_2 (top left), [Fe II] (top right), [Ar II] (bottom left) and [Ar III] (bottom right) for the five subsamples, as indicated by the different colors. These profiles are computed as median values of W_{80} and distance of the spaxel from the position of the continuum peak, within circular rings of 250 pc width. The numbers next to each point indicate the number of galaxies used to compute it, and the shaded regions represent the range between the 25th and 75th percentiles of the W_{80} values within each radial bin, illustrating the spread of values observed in each emission line
.

of increasing gas turbulence with distance from the nucleus, more evident for H_2 and [Fe II] (Fig. 5). RS AGN present more turbulent gas compared to other samples. (iii) There is a correlation between the width of the [Fe II] emission line and the line ratios H_2 S(5) $\lambda6.9091\,\mu$m/[Ar II] $\lambda6.9853\,\mu$m and [Fe II] $\lambda5.3403\,\mu$m/[Ar II] $\lambda6.9853\,\mu$m for all subsamples (Fig. 6). However, only AGN samples show a trend of increasing [Ar III] $\lambda8.9914\,\mu$m/[Ar II] $\lambda6.9853\,\mu$m with gas turbulence. In this section, we investigate the origin of the observed behavior in the W_{80} radial profiles and the physical mechanisms responsible for the line emission in our sample.

5.1. W_{80} radial profiles

When gas motions are governed by the gravitational potential, a decrease in velocity dispersion with increasing distance from the nucleus is expected; therefore, the observed W_{80} radial profiles in our sample cannot be solely explained by virial motions. Such profiles could be interpreted as being generated by outflows or associated with shocks that enhance the turbulence of the gas (e.g. Wylezalek et al. 2020; Ruschel-Dutra et al. 2021; Audibert et al. 2023; Bessiere et al. 2024). Similar increases in velocity dispersion with distance from the nucleus are observed in the inner few hundred parsecs of nearby AGN hosts, in both hot molecular gas (traced by the H_2 2.1218 μm line) and ionized gas (traced by the Brγ line), based on near-IR integral field spectroscopy observations of a sample of 31 AGN, in which KDRs are detected in 94% of the cases for the ionized gas and in 76% for the hot molecular gas (Riffel et al. 2023). A similar result is found using a larger sample of 88 AGN, in which flat or increasing velocity dispersion profiles are observed within the inner 200 pc for obscured, unobscured, and LINER sources,

including in the coronal gas traced by the [Si VI] 1.9641 μm emission line (Delaney et al. 2025). The origin of the enhanced line widths in these sources is associated with outflows and the shocks they produce (e.g. Riffel et al. 2021c). On galaxy-wide scales, AGN hosts exhibit enhanced velocity dispersion relative to normal galaxies, extending out to distances of up to 2 effective radii, as revealed by observations from the Mapping Nearby Galaxies at Apache Point Observatory (MaNGA) survey using the [O III] $\lambda5007$ emission line (Wylezalek et al. 2020; Albán et al. 2024). Radio-selected AGN exhibit the largest differences at all radii, indicating that AGN-driven kinematic perturbations in this population have been active for longer durations than in purely photoionized AGN, consistent with radio emission originating from shocks associated with outflows (Albán et al. 2024). On the other hand, Kukreti et al. (2025), using MaNGA data, find that radio AGN exhibit higher [O III] $\lambda5007$ velocity dispersions than optical AGN within the inner 0.5 effective radii, but show lower values at larger radii. These authors suggest that the discrepancy with the results of Albán et al. (2024) could be explained by the presence of low-luminosity AGN in their optical AGN sample, which are not included in the Albán et al. (2024) sample due to different selection methods. Despite the discrepancies at large distances from the nucleus, the results for the central regions of the galaxies, which are the focus of the present work, indicate that radio AGN exhibit higher gas turbulence.

Recently, Marconcini et al. (2025b) modeled the ionized gas kinematics of a sample of 10 galaxies observed with the Multi Unit Spectroscopic Explorer (MUSE), using the MOKA[3D] tool (Marconcini et al. 2023). They found that ionized outflows exhibit constant or slightly decreasing velocities within the inner 1 kpc from the nucleus, followed by a rapid increase, very similar to the behavior observed in our sample. Marconcini et al. (2025b) argue that the increase in outflow velocity, relative to
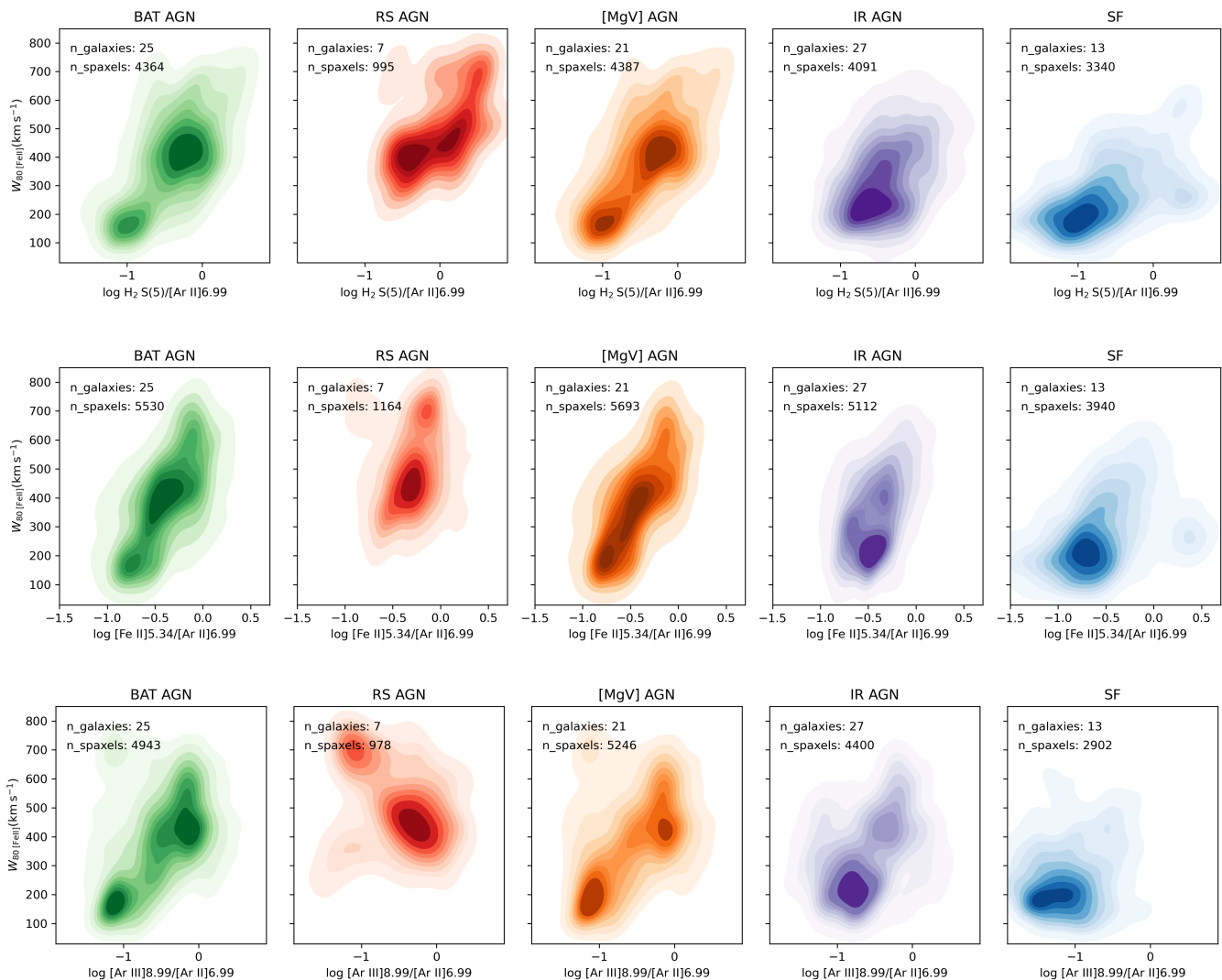
Fig. 6. Density maps of W_{80} for [Fe II] $\lambda5.3403\,\mu$m emission line as a function of the flux ratios: H$_2$ S(5) $\lambda6.9091\,\mu$m/[Ar II] $\lambda6.9853\,\mu$m (top panels), [Fe II] $\lambda5.3403\,\mu$m/[Ar II] $\lambda6.9853\,\mu$m (middle panels), and [Ar III] $\lambda8.9914\,\mu$m/[Ar II] $\lambda6.9853\,\mu$m (bottom panels). The contours are spaced at intervals of 10% in data density. Results are shown for the different subsamples, as identified in the title of each panel.

the galaxy escape velocity, is observed in the transition region, where a momentum-driven phase shifts to an energy-conserving phase beyond 1 kpc, with the outflow expanding as an isothermal, consistent with theoretical predictions of AGN outflows (e.g. King & Pounds 2015). Thus, the observed behavior of the W_{80} radial profiles in our sample, when compared with previous results, suggests that they are associated with AGN- or star-formation-driven energy-conserving winds capable of escaping the bulge of the galaxy, in both low-ionization and warm molecular gas phases. These findings indicate that the enhanced gas turbulence observed in our sample may play a significant role in the evolution of the host galaxies. However, a comprehensive analysis of the gas kinematics, including detailed modeling of individual sources, is required to fully characterize the outflow properties and assess their potential impact on SF.

5.2. Origin of the emission

The emission of [Fe II] is highly sensitive to shocks, increasing significantly when shocks release iron from dust grains (Oliva et al. 2001; Hashimoto et al. 2011; Aliste

Castillo et al. 2025). The emission of H$_2$ lines can also be enhanced in regions of shocked gas (Hollenbach & McKee 1989; Guillard et al. 2009; Kristensen et al. 2023; Appleton et al. 2023; Godard et al. 2024; Zanchettin et al. 2025). The [Ar III] $\lambda8.9914\,\mu$m/[Ar II] $\lambda6.9853\,\mu$m flux ratio can be used to map the ionization degree and the intensity of the incident radiation field in photoionized gas regions, as their parent ions have significantly different ionization potentials – 15.8 eV and 27.6 eV for Ar II and for Ar III, respectively. The observed trend of increasing W_{80} with increasing values of the H$_2$ S(5)/[Ar II]$\lambda6.9853\,\mu$m and [Fe II]$\lambda5.3403\,\mu$m/[Ar II]$\lambda6.9853\,\mu$m (first two rows of Fig. 6) could be interpreted as an additional contribution from shocks to the excitation of H$_2$ and [Fe II] emission lines. On the other hand, an increase in the [Ar III]$\lambda8.9914\,\mu$m/[Ar II]$\lambda6.9853\,\mu$m ratio for the larger W_{80}, seen for the AGN samples, might suggest that although part of the gas is in the outflow, it remains predominantly photoionized by the central AGN.

To further investigate the origin of gas turbulence and the trends observed in emission-line flux ratios, we present in Fig. 7 density plots for the [Fe II]$\lambda5.3403\,\mu$m/[Ar II]$\lambda6.9853\,\mu$m
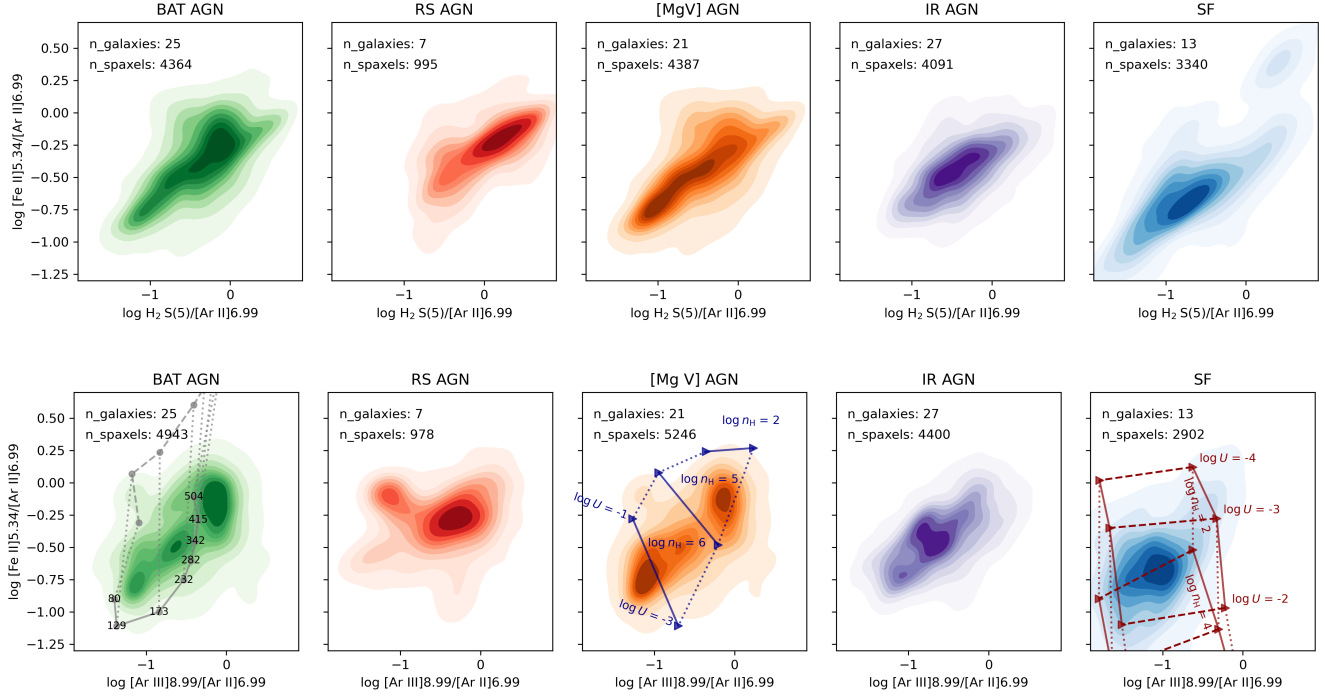
Fig. 7. Density plots for the [Fe ɪɪ]λ5.3403μm/[Ar ɪɪ]λ6.9853μm vs. H₂ S(5)/[Ar ɪɪ]λ6.9853μm (top panels) and [Fe ɪɪ]λ5.3403μm/[Ar ɪɪ]λ6.9853μm vs. [Ar ɪɪɪ]λ8.9914 μm/[Ar ɪɪ]λ6.9853 μm (bottom panels). The dark red lines (bottom-right panel) show predictions from photoionization models of star-forming regions, assuming stellar clusters aged 6 and 7 Myr. Solid lines indicate different gas densities, dotted lines correspond to varying ionization parameters (as labeled in the figure), and the predictions for both cluster ages are connected by dashed lines. Similarly, results from AGN photoionization models are shown as dark blue lines (bottom-central panel). The gray lines and filled circles (bottom-left panel) are predictions of fast shock models from Pereira-Santaella et al. (2024) using the ᴍᴀᴘᴘɪɴɢꜱ ᴠ code (Sutherland & Dopita 2017) for log R_P = 6 (dashed) and log R_P = 8 (continuous). The numbers indicate the shock velocities in km s⁻¹.
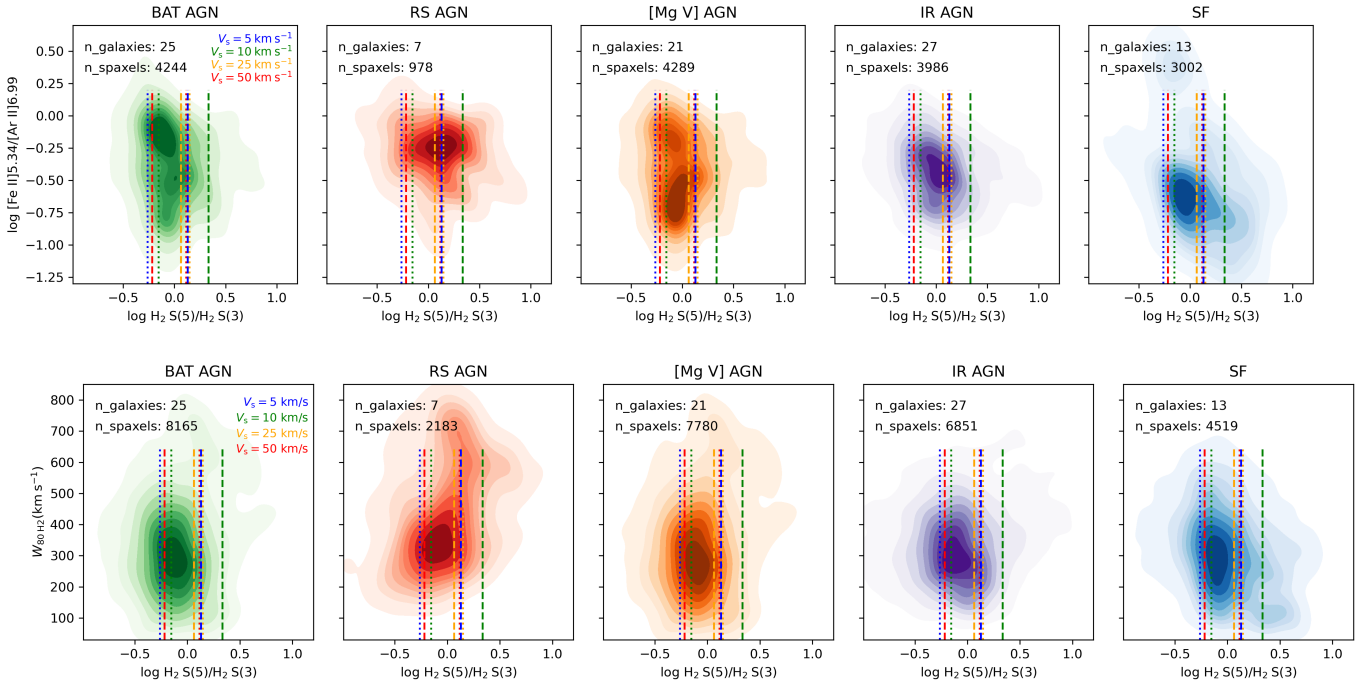
Fig. 8. Density plots for [Fe ɪɪ]λ5.3403 μm/[Ar ɪɪ]λ6.9853 μm vs. H₂ S(5)/H₂ S(3) (top) and W_{80} for the H₂ S(5) line vs. H₂ S(5)/H₂ S(3) (bottom) for all subsamples. The vertical lines represent mean H₂ S(5)/H₂ S(3) predictions of the shock models from Kristensen et al. (2023) for velocities of 5, 10, 25 and 50 km s⁻¹ (different colors) and densities of n_H = 10³ (dotted lines) and n_H = 10⁶ cm⁻¹ (dashed lines).

vs. H_2 S(5)/[Ar II]λ6.9853 μm (top panels) and [Fe II]λ5.3403 μm/[Ar II]λ6.9853 μm vs. [Ar III]λ8.9914 μm/[Ar II]λ6.9853 μm (bottom panels), for all subsamples. A strong correlation is observed for the first pair of intensity ratios in all samples, with Pearson correlation coefficients ranging from 0.53 to 0.76. As [Ar II] is predominantly produced by photoionization, while [Fe II] and H_2 are more sensitive to shocks, the observed correlation suggests that these latter lines trace shock-excited gas, particularly at larger distances from the nucleus. Moreover, the increase in line ratios with line widths (Fig. 6) provides strong evidence that the enhanced gas turbulence in these regions is driven by shocks. A much weaker trend is observed between [Fe II]λ5.3403 μm/[Ar II]λ6.9853 μm and [Ar III]λ8.9914 μm/[Ar II]λ6.9853 μm, and only for the AGN samples (excluding the RS AGN). No clear relationship is observed between these line ratios for the SF subsample, where argon emission is attributed to SF. Since the [Fe II] and H_2 fluxes increase relative to [Ar II] emission and also increase with line width, this suggests that both [Fe II] and H_2 exhibit enhanced emission due to shocks, which could be associated with stellar winds and mergers. This is consistent with the fact that the SF subsample is predominantly composed of U/LIRGs, which are known for intense SF activity and their presence in merger systems. Similarly, no clear relationship is observed between these line ratios for the RS AGN sample. In this case, the possible origin of the shocked [Fe II] and H_2 gas may be associated with radio emission, stellar winds, or interactions in the U/LIRGs of this subsample.

We can compare the observed emission-line ratios with predictions from shock and photoionization models. The results from fast shock models by Pereira-Santaella et al. (2024), using the MAPPINGS V code (Dopita & Sutherland 1996; Sutherland & Dopita 2017), are shown overlaid as gray lines in the bottom-left panel of Fig. 7. A short description of these models are presented in Appendix D. Although these authors produced an extensive grid of models (see their work for more details), we only show a subset in the figure to avoid overcrowding. The displayed models assume solar metallicity, shock velocities (v_s) ranging from 80 to 500 km s^{-1}, and ram pressure parameters defined as $R_P = \frac{n_H}{cm^{-3}} \times \left(\frac{v_s}{km/s}\right)^2$, with values of 10^6 and 10^8, where n_H is the gas volume density. We also constructed extensive photoionization model grids for AGN and SF using the CLOUDY code (Ferland et al. 2017), as detailed in Appendix D. The SF models are shown as dark red lines in the bottom-right panel of Fig. 7. We present predictions for gas densities of $\log(n_H/cm^{-3}) = 2$ and 4, and ionization parameters of $\log U = -4, -3,$ and -2, based on Spectral Energy Distributions (SEDs) generated with the STARBURST99 code (Leitherer et al. 1999) for stellar clusters aged 6 Myr (yielding higher [Ar III]/[Ar II] ratios) and 7 Myr (lower ratios). These models are able to reproduce the lower line ratios, supporting a interpretation that they originate from gas photoionized by young stellar populations. The predictions from AGN photoionization models are shown as blue lines in the bottom-central panel of Fig. 7, for densities of $\log(n_H/cm^{-3}) = 2, 5,$ and 6, and ionization parameters of $\log U = -1$ and -3. These models are able to reproduce the highest line ratios, including the extreme [Ar III]/[Ar II] values observed, which are not well matched by the shock models.

As shown, the observed [Fe II]λ5.3403 μm/[Ar II]λ6.9853 μm flux ratios align well with the values predicted by shock models. In contrast, the [Ar III] λ8.9914 μm/[Ar II] λ6.9853 μm ratios exhibit values higher than those predicted by shock models, but are well reproduced by AGN photoionization models. In addition,

the lowest values of both ratios are consistent with predictions from SF photoionization models.

Fig. 8 displays density plots of [Fe II]λ5.3403 μm/[Ar II]λ6.9853 μm and W_{80} of the H_2 S(5) line against the H_2 S(5)/H_2 S(3) line ratio, which is a tracer of the H_2 temperature and is enhanced in shock dominated-regions (e.g. Zakamska 2010; Pereira-Santaella et al. 2014; Togi & Smith 2016; Dan et al. 2025; Riffel et al. 2025). The observed values for this ratio are consistent with those predicted by low velocity shock models (2–90 km s^{-1}), as indicated by the vertical lines representing predictions by the models from Kristensen et al. (2023). However, no evident correlation is observed. This indicates that if the H_2 emission is produced by shocks, these are not the same shocks responsible for the [Fe II] emission (Hollenbach & McKee 1989; Mouri et al. 2000; Allen et al. 2008). This is expected, as the shock waves produced by fast shocks with velocities of $200 - 300$ km s^{-1} necessary to generate ionized gas emission would lead to the dissociation of H_2 molecules. On the other hand, the tight correlation observed between the [Fe II] and H_2 emission (top row of Fig. 7) indicates that they share the same physical origin. A possible interpretation for this correlation is that the H_2 emission originates in the post-shock gas, where the molecules reform after being dissociated by the fast shock (Guillard et al. 2009; Richings & Faucher-Giguère 2018b,a). Another explanation is the excitation of H_2 in the molecular shock precursor, as observed in NGC 7319. In this case, the ionized gas is significantly more turbulent than the molecular gas, with $\sigma \approx 300$ km s^{-1} for the ionized gas and $\sigma \approx 150$ km s^{-1} for the H_2, in regions co-spatial with a radio hotspot (Pereira-Santaella et al. 2022). Although the W_{80} values for H_2 are typically lower than those for the ionized gas (Fig. 4), the radial profiles of W_{80} for H_2 and [Fe II] show similar trends, with values increasing from the nucleus outward, suggesting that the first interpretation is more likely.

The analysis of emission line ratios, gas kinematics, and comparisons with shock and photoionization models indicates that shocks driven by outflows and jets are a key factor in producing the [Fe II] and H_2 emission within the inner few kpc of AGN host galaxies. The [Fe II] emission arises from partially ionized zones situated beyond the main hydrogen ionization front in narrow-line region clouds, forming a transition between fully ionized and neutral gas (Forbes & Ward 1993; Simpson et al. 1996), while the mid-IR H_2 lines trace warm molecular gas at temperatures of a few hundred Kelvin (Pereira-Santaella et al. 2014; Togi & Smith 2016). Our results suggest that turbulence produced in the ISM by outflows and/or radio jets may constitute an important mechanism of maintenance-mode AGN feedback, as it prevents the gas from efficiently cooling and forming stars, thus regulating star formation.

6. Conclusions

We have used archival JWST MIRI/MRS observations of a sample consisting of 54 galaxies at $z < 0.1$ to investigate the origin of the warm molecular and low-ionization gas emission. The sample includes SFGs and AGN hosts, with AGN selected based on their X-ray, radio, and coronal line emissions. We investigate the origin of the emission and turbulence of the gas from flux measurements and velocity dispersion, parameterized by the W_{80} parameter, for H_2 S(5)λ6.9091μm, [Ar II]λ6.9853μm, [Fe II]λ5.3403μm, [Ar III]λ8.9914μm, and [Mg V]λ5.6098μm emission lines. Our main conclusions are the following:

- AGN exhibit broader emission lines than SFGs, with the largest velocity dispersions observed for radio-strong AGN. The H_2 gas is less turbulent compared to the ionized gas for all the subsamples studied, followed by [Ar II], [Ar III], and [Fe II]. Among the galaxies with coronal emission, the coronal gas shows higher velocity dispersion values compared to lower-ionization lines, suggesting stratified emission clouds.
- The velocity dispersion of molecular and low-ionization gas increases with distance from the nucleus, particularly for the emission lines of H_2 and [Fe II], which is contrary to what is expected from gravitationally dominated motions. Additionally, the high values of W_{80} indicate the presence of outflows in AGN hosts, while in SF, the W_{80} values are lower than those for AGN, yet still require an additional component, such as shock-heated gas emission from stellar winds or galaxy interactions.
- There is a strong correlation between the W_{80} parameter and the line ratios H_2 S(5)$\lambda6.9091\mu m$/[Ar II]$\lambda6.9853\mu m$ and [Fe II]$\lambda5.3403\mu m$/[Ar II]$\lambda6.9853\mu m$, as well as between these two ratios themselves. This indicates that the [Fe II] and H_2 emissions originate from linked physical processes. Since H_2 and [Fe II] emissions are enhanced in shocked gas, these correlations provide additional evidence that shocks play an important role in the observed emission in our sample.
- The lowest W_{80} values (<300 km s^{-1}) across all samples are associated with SF, presenting line ratios consistent with predictions from SF photoionization models for gas densities in the range 10^2–10^4 cm^{-3}. As gas turbulence increases, the contribution from shocks becomes significant, with [Fe II]$\lambda5.3403\mu m$/[Ar II]$\lambda6.9853\mu m$ intensity ratios consistent with predictions from fast shock models, assuming shock velocities in the range of ~ 100 to ~ 300 km s^{-1} and gas densities between 10^3 and 10^4 cm^{-3}. Some contribution from AGN photoionization may be important, particularly for the highest [Ar III] $\lambda8.9914\mu m$/[Ar II] $\lambda6.9853\mu m$ ratios, which are consistent with AGN photoionization models for gas densities of 10^2 and 10^5 cm^{-3}.
- Although the observed H_2 S(5)/H_2 S(3) flux line ratios are consistent with predictions of slow shock models, there is no trend between this line ratio and the H_2 velocity dispersion and [Fe II]$\lambda5.3403\mu m$/[Ar II]$\lambda6.9853\mu m$. These results, along with the similar trends observed in the gas turbulence for [Fe II] and H_2, increasing from the nucleus outwards, leads to the interpretation that the H_2 emission could be produced by molecules reforming in the post-shock region.
- We find similarities in line widths and line ratios between the BAT and [Mg V] AGN subsamples, consistent with the fact that both are direct tracers of AGN emission, whether through the X-rays generated by the central engine or the high-energy photons necessary to ionize the coronal gas. Similarly, among the AGN subsamples, the IR AGN subsample shows line widths and ratios more closely resembling those of the SFGs, consistent with many IR AGN being U/LIRGs that exhibit intense star formation.

Our analysis reveals that high turbulence is a pervasive feature present in all the subsamples studied. This turbulence, driven by AGN outflows/jets and/or stellar winds, plays a crucial role in influencing the kinematics and physical state of the ISM in these galaxies. The widespread presence of such energetic feedback mechanisms underscores their importance in galaxy evolution, affecting gas dynamics and potentially regulating SF across diverse environments.

References

Albán, M., Wylezalek, D., Comerford, J. M., Greene, J. E., & Riffel, R. A. 2024, A&A, 691, A124

Aliste Castillo, R. L. S. E., Lee, Y.-H., Kokusho, T., et al. 2025, AJ, 169, 227

Allen, M. G., Groves, B. A., Dopita, M. A., Sutherland, R. S., & Kewley, L. J. 2008, ApJS, 178, 20

Allison, J. R., Sadler, E. M., & Meekin, A. M. 2014, MNRAS, 440, 696

Alonso-Herrero, A., García-Burillo, S., Hönig, S. F., et al. 2021, A&A, 652, A99

Alonso Herrero, A., Hermosa Muñoz, L., Labiano, A., et al. 2024, A&A, 690, A95

Alonso-Herrero, A., Hermosa Muñoz, L., Labiano, A., et al. 2025, arXiv e-prints, arXiv:2506.15286

Antonucci, R. 1993, ARA&A, 31, 473

Appleton, P. N., Guillard, P., Emonts, B., et al. 2023, ApJ, 951, 104

Appleton, P. N., Guillard, P., Togi, A., et al. 2017, ApJ, 836, 76

Argyriou, I., Glasse, A., Law, D. R., et al. 2023, A&A, 675, A111

Armus, L., Lai, T., U, V., et al. 2023, ApJ, 942, L37

Armus, L., Mazzarella, J. M., Evans, A. S., et al. 2009, PASP, 121, 559

Arribas, S., Colina, L., Bellocchi, E., Maiolino, R., & Villar-Martín, M. 2014, A&A, 568, A14

Assef, R. J., Kochanek, C. S., Brodwin, M., et al. 2010, ApJ, 713, 970

Astropy Collaboration, Price-Whelan, A. M., Lim, P. L., et al. 2022, ApJ, 935, 167

Astropy Collaboration, Robitaille, T. P., Tollerud, E. J., et al. 2013, A&A, 558, A33

Audibert, A., Ramos Almeida, C., García-Burillo, S., et al. 2023, A&A, 671, L12

Audibert, A., Ramos Almeida, C., García-Burillo, S., et al. 2025, A&A, 699, A83

Avery, C. R., Wuyts, S., Förster Schreiber, N. M., et al. 2021, MNRAS, 503, 5134

Baan, W. A. & Klöckner, H. R. 2006, A&A, 449, 559

Baldwin, J. A., Phillips, M. M., & Terlevich, R. 1981, PASP, 93, 5

Becker, R. H., White, R. L., & Edwards, A. L. 1991, ApJS, 75, 1

Bellocchi, E., Arribas, S., Colina, L., & Miralles-Caballero, D. 2013, A&A, 557, A59

Bessiere, P. S. & Ramos Almeida, C. 2022, MNRAS, 512, L54

Bessiere, P. S., Ramos Almeida, C., Holden, L. R., Tadhunter, C. N., & Canalizo, G. 2024, A&A, 689, A271

Best, P. N., Kauffmann, G., Heckman, T. M., et al. 2005, MNRAS, 362, 25

Bianchin, M., Riffel, R. A., Storchi-Bergmann, T., et al. 2022, MNRAS, 510, 639

Biémont, E., Frémat, Y., & Quinet, P. 1999, Atomic Data and Nuclear Data Tables, 71, 117

Bohn, T., Inami, H., Togi, A., et al. 2024, ApJ, 977, 36

Bottinelli, L., Gouguenheim, L., Paturel, G., & de Vaucouleurs, G. 1984, A&AS, 56, 381

Bressan, A., Fagotto, F., Bertelli, G., & Chiosi, C. 1993, A&AS, 100, 647

Brown, M. J. I., Moustakas, J., Kennicutt, R. C., et al. 2017, ApJ, 847, 136

Buiten, V. A., van der Werf, P. P., Viti, S., et al. 2024, ApJ, 966, 166

Bushouse, H., Eisenhamer, J., Dencheva, N., et al. 2024, JWST Calibration Pipeline

Cassanta, C. M., Riffel, R. A., Robinson, A., et al. 2025, MNRAS, 541, 266

Ceci, M., Marconcini, C., Marconi, A., et al. 2025, arXiv e-prints, arXiv:2507.08077

Chatzikos, M., Bianchi, S., Camilloni, F., et al. 2023, Rev. Mexicana Astron. Astrofís., 59, 327

Cicone, C., Maiolino, R., Sturm, E., et al. 2014, A&A, 562, A21

Cluver, M. E., Jarrett, T. H., Dale, D. A., et al. 2017, ApJ, 850, 68

Colina, L., Piqueras López, J., Arribas, S., et al. 2015, A&A, 578, A48

Condon, J. J., Cotton, W. D., & Broderick, J. J. 2002, AJ, 124, 675

Condon, J. J., Cotton, W. D., Greisen, E. W., et al. 1998, AJ, 115, 1693

Condon, J. J., Helou, G., Sanders, D. B., & Soifer, B. T. 1996, ApJS, 103, 81

Contini, M. & Viegas, S. M. 2001, ApJS, 132, 211

Costa-Souza, J. H., Riffel, R. A., Souza-Oliveira, G. L., et al. 2024, ApJ, 974, 127

Cresci, G., Marconi, A., Zibetti, S., et al. 2015, A&A, 582, A63

Dalla Vecchia, C. & Schaye, J. 2012, MNRAS, 426, 140

Dan, K. Y., Seebeck, J., Veilleux, S., et al. 2025, ApJ, 979, 68

Dasyra, K. M., Paraschos, G. F., Combes, F., et al. 2024, ApJ, 977, 156

Davies, R., Shimizu, T., Pereira-Santaella, M., et al. 2024, A&A, 689, A263

Davies, R. I., Burtscher, L., Rosario, D., et al. 2015, ApJ, 806, 127

Deconto-Machado, A., Riffel, R. A., Ilha, G. S., et al. 2022, A&A, 659, A131

Delaney, D., Berger, C., Hicks, E., et al. 2025, ApJ, 984, 163

Di Matteo, T., Springel, V., & Hernquist, L. 2005, Nature, 433, 604

Done, C., Davis, S. W., Jin, C., Blaes, O., & Ward, M. 2012, MNRAS, 420, 1848

Dopita, M. A. & Sutherland, R. S. 1995, ApJ, 455, 468

Dopita, M. A. & Sutherland, R. S. 1996, ApJS, 102, 161

Dors, O. L., Contini, M., Riffel, R. A., et al. 2021, MNRAS, 501, 1370

Dors, Jr., O. L., Riffel, R. A., Cardaci, M. V., et al. 2012, MNRAS, 422, 252

Draine, B. T., Dale, D. A., Bendo, G., et al. 2007, ApJ, 663, 866

Emonts, B. H. C., Colina, L., Piqueras-López, J., et al. 2017, A&A, 607, A116

Epinat, B., Amram, P., Balkowski, C., & Marcelin, M. 2010, MNRAS, 401, 2113

Esposito, F., Alonso-Herrero, A., García-Burillo, S., et al. 2024, A&A, 686, A46

Evans, A. S., Frayer, D. T., Charmandaris, V., et al. 2022, ApJ, 940, L8

Ferland, G. J., Chatzikos, M., Guzmán, F., et al. 2017, Rev. Mexicana Astron. Astrofís., 53, 385

Fierlinger, K. M., Burkert, A., Ntormousi, E., et al. 2016, MNRAS, 456, 710

Fischer, T. C., Kraemer, S. B., Schmitt, H. R., et al. 2018, ApJ, 856, 102

Forbes, D. A. & Ward, M. J. 1993, ApJ, 416, 150

Förster Schreiber, N. M., Übler, H., Davies, R. L., et al. 2019, ApJ, 875, 21

Freitas, I. C., Riffel, R. A., Storchi-Bergmann, T., et al. 2018, MNRAS, 476, 2760

Gallagher, R., Maiolino, R., Belfiore, F., et al. 2019, MNRAS, 485, 3409

García-Bernete, I., Alonso-Herrero, A., García-Burillo, S., et al. 2021, A&A, 645, A21

García-Bernete, I., Alonso-Herrero, A., Rigopoulou, D., et al. 2024a, A&A, 681, L7

García-Bernete, I., Donnan, F. R., Rigopoulou, D., et al. 2025, A&A, 696, A135

García-Bernete, I., Rigopoulou, D., Donnan, F. R., et al. 2024b, A&A, 691, A162

García-Burillo, S., Alonso-Herrero, A., Ramos Almeida, C., et al. 2021, A&A, 652, A98

Gardner, J. P., Mather, J. C., Abbott, R., et al. 2023, PASP, 135, 068001

Gatto, L., Storchi-Bergmann, T., Riffel, R. A., et al. 2024, MNRAS, 530, 3059

Gerke, J. R., Kochanek, C. S., Prieto, J. L., Stanek, K. Z., & Macri, L. M. 2011, ApJ, 743, 176

Godard, B., des Forêts, G. P., & Bialy, S. 2024, A&A, 688, A169

Gordon, K. D., Clayton, G. C., Decleir, M., et al. 2023, ApJ, 950, 86

Gregory, P. C. & Condon, J. J. 1991, ApJS, 75, 1011

Gregory, P. C., Scott, W. K., Douglas, K., & Condon, J. J. 1996, ApJS, 103, 427

Grevesse, N., Asplund, M., Sauval, A. J., & Scott, P. 2010, Ap&SS, 328, 179

Griffith, M. R., Wright, A. E., Burke, B. F., & Ekers, R. D. 1994, ApJS, 90, 179

Guillard, P., Boulanger, F., Pineau Des Forêts, G., & Appleton, P. N. 2009, A&A, 502, 515

Harrison, C. M. 2017, Nature Astronomy, 1, 0165

Harrison, C. M. & Ramos Almeida, C. 2024, Galaxies, 12, 17

Hashimoto, T., Nagao, T., Yanagisawa, K., Matsuoka, K., & Araki, N. 2011, PASJ, 63, L7

Heckman, T. M. & Best, P. N. 2014, ARA&A, 52, 589

Hermosa Muñoz, L., Alonso-Herrero, A., Labiano, A., et al. 2025, A&A, 693, A321

Hermosa Muñoz, L., Alonso-Herrero, A., Pereira-Santaella, M., et al. 2024, A&A, 690, A350

Hill, M. J. & Zakamska, N. L. 2014, MNRAS, 439, 2701

Hoffmann, S. L. & Macri, L. M. 2015, AJ, 149, 183

Hollenbach, D. & McKee, C. F. 1989, ApJ, 342, 306

Hopkins, P. F., Quataert, E., & Murray, N. 2012, MNRAS, 421, 3522

Izotov, Y. I., Stasińska, G., Meynet, G., Guseva, N. G., & Thuan, T. X. 2006, A&A, 448, 955

Jarrett, T. H., Cohen, M., Masci, F., et al. 2011, ApJ, 735, 112

Jin, C., Ward, M., & Done, C. 2012, MNRAS, 425, 907

Jones, O. C., Álvarez-Márquez, J., Sloan, G. C., et al. 2023, MNRAS, 523, 2519

Jose, C., Chamandy, L., Shukurov, A., et al. 2024, MNRAS, 532, 1504

Kakkad, D., Sani, E., Rojas, A. F., et al. 2022, MNRAS, 511, 2105

Karachentsev, I. D., Karachentseva, V. E., & Nasonova, O. G. 2014, Astrophysics, 57, 457

Kaufman, V. & Whaling, W. 1996, J. Res. Natl. Inst. Stand. Technol., 101, 691

Kellermann, K. I., Sramek, R., Schmidt, M., Shaffer, D. B., & Green, R. 1989, AJ, 98, 1195

King, A. & Pounds, K. 2015, ARA&A, 53, 115

Kramida, A., Ralchenko, Y., & Reader, J. 2014, in APS Division of Atomic, Molecular and Optical Physics Meeting Abstracts, APS Meeting Abstracts, D1.047

Kristensen, L. E., Godard, B., Guillard, P., Gusdorf, A., & Pineau des Forêts, G. 2023, A&A, 675, A86

Kroupa, P. 2002, Science, 295, 82

Kukreti, P., Wylezalek, D., Albán, M., & Dall'Agnol de Oliveira, B. 2025, A&A, 698, A99

Labiano, A., Argyriou, I., Álvarez-Márquez, J., et al. 2021, A&A, 656, A57

Law, D. R., E. Morrison, J., Argyriou, I., et al. 2023, AJ, 166, 45

Leftley, J. H., Nesvadba, N. P. H., Bicknell, G. V., et al. 2024, A&A, 689, A314

Leitherer, C., Schaerer, D., Goldader, J. D., et al. 1999, ApJS, 123, 3

Maiolino, R., Russell, H. R., Fabian, A. C., et al. 2017, Nature, 544, 202

Majaess, D. J., Turner, D. G., & Lane, D. J. 2008, MNRAS, 390, 1539

Marconcini, C., Feltre, A., Lamperti, I., et al. 2025a, A&A, 701, A113

Marconcini, C., Marconi, A., Cresci, G., et al. 2025b, Nature Astronomy [arXiv:2503.24359]

Marconcini, C., Marconi, A., Cresci, G., et al. 2023, A&A, 677, A58

Mouri, H., Kawara, K., & Taniguchi, Y. 2000, ApJ, 528, 186

Mullaney, J. R., Alexander, D. M., Fine, S., et al. 2013, MNRAS, 433, 622

Nagar, N. M., Falcke, H., & Wilson, A. S. 2005, A&A, 435, 521

Nasonova, O. G., de Freitas Pacheco, J. A., & Karachentsev, I. D. 2011, A&A, 532, A104

Nave, G. & Johansson, S. 2013, ApJS, 204, 1

Negus, J., Comerford, J. M., Sánchez, F. M., et al. 2023, ApJ, 945, 127

Netzer, H. 2015, ARA&A, 53, 365

Ogle, P., Boulanger, F., Guillard, P., et al. 2010, ApJ, 724, 1193

Ogle, P. M., Sebastian, B., Aravindan, A., et al. 2025, arXiv e-prints, arXiv:2502.06603

Oh, K., Koss, M., Markwardt, C. B., et al. 2018, ApJS, 235, 4

Ohyama, Y., Terashima, Y., & Sakamoto, K. 2015, ApJ, 805, 162

Oldham, L. J. & Auger, M. W. 2016, MNRAS, 455, 820

Oliva, E., Marconi, A., Maiolino, R., et al. 2001, A&A, 369, L5

Orienti, M. & Prieto, M. A. 2010, MNRAS, 401, 2599

Padovani, P. 2017, Frontiers in Astronomy and Space Sciences, 4, 35

Pereira-Santaella, M., Álvarez-Márquez, J., García-Bernete, I., et al. 2022, A&A, 665, L11

Pereira-Santaella, M., García-Bernete, I., González-Alfonso, E., et al. 2024, A&A, 685, L13

Pereira-Santaella, M., Spinoglio, L., van der Werf, P. P., & Piqueras López, J. 2014, A&A, 566, A49

Perna, M., Arribas, S., Colina, L., et al. 2022, A&A, 662, A94

Piqueras López, J., Colina, L., Arribas, S., Alonso-Herrero, A., & Bedregal, A. G. 2012, A&A, 546, A64

Radburn-Smith, D. J., de Jong, R. S., Seth, A. C., et al. 2011, ApJS, 195, 18

Radcliffe, J. F., Barthel, P. D., Thomson, A. P., et al. 2021, A&A, 649, A27

Ramos Almeida, C., Acosta-Pulido, J. A., Tadhunter, C. N., et al. 2019, MNRAS, 487, L18

Ramos Almeida, C., García-Bernete, I., Pereira-Santaella, M., et al. 2025, A&A, 698, A194

Ramos Almeida, C., Piqueras López, J., Villar-Martín, M., & Bessiere, P. S. 2017, MNRAS, 470, 964

Rest, A., Scolnic, D., Foley, R. J., et al. 2014, ApJ, 795, 44

Ricci, T. V., Steiner, J. E., May, D., Garcia-Rissmann, A., & Menezes, R. B. 2018, MNRAS, 473, 5334

Richings, A. J. & Faucher-Giguère, C.-A. 2018a, MNRAS, 478, 3100

Richings, A. J. & Faucher-Giguère, C.-A. 2018b, MNRAS, 474, 3673

Riess, A. G., Macri, L. M., Hoffmann, S. L., et al. 2016, ApJ, 826, 56

Riffel, R. A., Bianchin, M., Riffel, R., et al. 2021a, MNRAS, 503, 5161

Riffel, R. A., Dors, O. L., Armah, M., et al. 2021b, MNRAS, 501, L54

Riffel, R. A., Souza-Oliveira, G. L., Costa-Souza, J. H., et al. 2025, ApJ, 982, 69

Riffel, R. A., Storchi-Bergmann, T., Riffel, R., et al. 2023, MNRAS, 521, 1832

Riffel, R. A., Storchi-Bergmann, T., Riffel, R., et al. 2021c, MNRAS, 504, 3265

Rodríguez-Ardila, A. & Cerqueira-Campos, F. 2025, Frontiers in Astronomy and Space Sciences, 12, 1548632

Rodríguez-Ardila, A., Fonseca-Faria, M. A., Dahmer-Hahn, L. G., et al. 2025, MNRAS, 538, 2800

Ruschel-Dutra, D., Storchi-Bergmann, T., Schnorr-Müller, A., et al. 2021, MNRAS, 507, 74

Sabbi, E., Calzetti, D., Ubeda, L., et al. 2018, ApJS, 235, 23

Sajina, A., Partridge, B., Evans, T., et al. 2011, ApJ, 732, 45

Sansonetti, J. E. & Martin, W. C. 2005, Journal of Physical and Chemical Reference Data, 34, 1559

Schönell, Jr., A. J., Riffel, R. A., Riffel, R., & Storchi-Bergmann, T. 2025, MNRAS, 537, 3826

Silk, J. 2013, ApJ, 772, 112

Silk, J., Begelman, M. C., Norman, C., Nusser, A., & Wyse, R. F. G. 2024, ApJ, 961, L39

Silk, J. & Rees, M. J. 1998, A&A, 331, L1

Simpson, C., Forbes, D. A., Baker, A. C., & Ward, M. J. 1996, MNRAS, 283, 777

Skrutskie, M. F., Cutri, R. M., Stiening, R., et al. 2006, AJ, 131, 1163

Speranza, G., Ramos Almeida, C., Acosta-Pulido, J. A., et al. 2024, A&A, 681, A63

Spitler, L. R., Larsen, S. S., Strader, J., et al. 2006, AJ, 132, 1593

Steenbrugge, K. C., Heywood, I., & Blundell, K. M. 2010, MNRAS, 401, 67

Stern, D., Assef, R. J., Benford, D. J., et al. 2012, ApJ, 753, 30

Stil, J. M., Krause, M., Beck, R., & Taylor, A. R. 2009, ApJ, 693, 1392

Su, R., Mahony, E. K., Gu, M., et al. 2023, MNRAS, 520, 5712

Sutherland, R. S. & Dopita, M. A. 2017, ApJS, 229, 34

Tadhunter, C. 2016, A&A Rev., 24, 10

Tingay, S. J., Jauncey, D. L., King, E. A., et al. 2003, PASJ, 55, 351

Togi, A. & Smith, J. D. T. 2016, ApJ, 830, 18

Tully, R. B., Courtois, H. M., Dolphin, A. E., et al. 2013, AJ, 146, 86

Tully, R. B., Courtois, H. M., & Sorce, J. G. 2016, AJ, 152, 50

U, V., Lai, T., Bianchin, M., et al. 2022, ApJ, 940, L5

Veilleux, S., Maiolino, R., Bolatto, A. D., & Aalto, S. 2020, A&A Rev., 28, 2

Venturi, G., Cresci, G., Marconi, A., et al. 2021, A&A, 648, A17

Villar Martín, M., Castro-Rodríguez, N., Pereira Santaella, M., et al. 2023, A&A, 673, A25

Wells, M., Pel, J. W., Glasse, A., et al. 2015, PASP, 127, 646

Willick, J. A., Courteau, S., Faber, S. M., et al. 1997, ApJS, 109, 333

Wright, A. E., Griffith, M. R., Burke, B. F., & Ekers, R. D. 1994, ApJS, 91, 111

Wright, E. L., Eisenhardt, P. R. M., Mainzer, A. K., et al. 2010, AJ, 140, 1868

Wright, G. S., Rieke, G. H., Glasse, A., et al. 2023, PASP, 135, 048003

Wright, G. S., Wright, D., Goodson, G. B., et al. 2015, PASP, 127, 595

Wylezalek, D., Flores, A. M., Zakamska, N. L., Greene, J. E., & Riffel, R. A. 2020, MNRAS, 492, 4680

Zakamska, N. L. 2010, Nature, 465, 60

Zakamska, N. L., Lampayan, K., Petric, A., et al. 2016, MNRAS, 455, 4191

Zanchettin, M. V., Massardi, M., Salvestrini, F., et al. 2024, ApJ, 970, 75

Zanchettin, M. V., Ramos Almeida, C., Audibert, A., et al. 2025, A&A, 695, A185

Zhang, L., Packham, C., Hicks, E. K. S., et al. 2024, ApJ, 974, 195

Zubovas, K. & King, A. R. 2014, MNRAS, 439, 400

[1] Centro de Astrobiología (CAB), CSIC-INTA, Ctra. de Ajalvir km 4, Torrejón de Ardoz, E-28850, Madrid, Spain

[2] Departamento de Física, CCNE, Universidade Federal de Santa Maria, Av. Roraima 1000, 97105-900, Santa Maria, RS, Brazil

[3] European Southern Observatory, Karl-Schwarzschild-Strasse 2, Garching bei München, Germany

[4] Instituto de Física Fundamental, CSIC, Calle Serrano 123, E-28006 Madrid, Spain

[5] Universidade do Vale do Paraíba, Av. Shishima Hifumi, 2911, Cep 12244-000, São José dos Campos, SP, Brazil

[6] Centro de Astrobiología (CAB), CSIC-INTA, Camino Bajo del Castillo s/n, E-28692, Villanueva de la Cañada, Madrid, Spain

[7] Instituto de Astrofísica de Canarias, Calle Vía Láctea, s/n, E-38205, La Laguna, Tenerife, Spain

[8] Departamento de Astrofísica, Universidad de La Laguna, E-38206, La Laguna, Tenerife, Spain

[9] Departmento de Física de la Tierra y Astrofísica, Fac. de CC Físicas, Universidad Complutense de Madrid, E-28040 Madrid, Spain

[10] Instituto de Física de Partículas y del Cosmos IPARCOS, Fac. CC Físicas, Universidad Complutense de Madrid, E-28040 Madrid, Spain

[11] Department of Physics, University of Oxford, Denys Wilkinson Building, Keble Road, Oxford OX1 3RH, UK

[12] School of Mathematics, Statistics, and Physics, Newcastle University, Newcastle upon Tyne NE1 7RU, UK

[13] Observatoire de Paris, LUX, PSL University, Sorbonne Université, CNRS, F-75014 Paris, France

[14] Collège de France, 11 Place Marcelin Berthelot, 75231 Paris, France

[15] Max-Planck-Institut für Extraterrestrische Physik, Postfach 1312, 85741 Garching, Germany

[16] Institute of Astrophysics, Foundation for Research and Technology-Hellas, 71110 Heraklion, Greece

[17] School of Sciences, European University Cyprus, Diogenes Street, Engomi 1516, Nicosia, Cyprus

[18] Center for Astrophysics & Space Sciences, Department of Physics, University of California San Diego, 9500 Gilman Drive, San Diego, CA 92093, USA

[19] Observatorio de Madrid, OAN-IGN, Alfonso XII, 3, E-28014 Madrid, Spain

[20] Instituto de Radioastronomía y Astrofísica (IRyA), Universidad Nacional Autónoma de México, Antigua Carretera a Pátzcuaro #8701, Ex-Hda. San José de la Huerta, C.P. 58089 Morelia, Michoacán, Mexico

[21] Department of Physics & Astronomy, University of Alaska Anchorage, Anchorage, AK 99508-4664, USA

[22] Department of Physics, University of Alaska, Fairbanks, Alaska 99775-5920, USA

[23] Department of Physics & Astronomy, The University of Texas at San Antonio, One UTSA Circle, San Antonio, TX 78249, USA

[24] School of Physics & Astronomy, University of Southampton, Southampton SO17 1BJ, UK

[25] National Astronomical Observatory of Japan, National Institutes of Natural Sciences (NINS), 2-21-1 Osawa, Mitaka, Tokyo 181-8588, Japan

[26] Department of Astronomy, School of Science, Graduate University for Advanced Studies (SOKENDAI), Mitaka, Tokyo 181-8588, Japan

[27] Telespazio UK for the European Space Agency (ESA), ESAC, Camino Bajo del Castillo s/n, 28692, Villanueva de la Cañada, Spain

[28] Department of Physics & Astronomy, University of South Carolina, Columbia, SC 29208, USA

[29] Kavli Institute for Particle Astrophysics & Cosmology (KIPAC), Stanford University, Stanford, CA 94305, USA

[30] Department of Physics, University of Oxford, Keble Road, Oxford OX1 3RH, UK

[31] School of Sciences, European University Cyprus, Diogenes street, Engomi, 1516 Nicosia, Cyprus

Appendix A: Observational proposals

Our sample consists of 54 galaxies, listed in Table A.1, along with details of the observational proposals. Our sample includes representatives from the The Great Observatories All-Sky LIRG Survey (GOALS; e.g. Armus et al. 2009; U et al. 2022; Evans et al. 2022; Buiten et al. 2024), The Galaxy Activity, Torus, and Outflow Survey (GATOS; e.g. García-Burillo et al. 2021; Alonso-Herrero et al. 2021; Davies et al. 2024; García-Bernete et al. 2024a), Mid-IR Characterization Of Nearby Iconic galaxy Centers (MICONIC; e.g. Alonso Herrero et al. 2024; Alonso-Herrero et al. 2025; Hermosa Muñoz et al. 2025), Mid-InfraRed Activity of Circumnuclear Line Emission (MIRACLE; e.g. Marconcini et al. 2025a; Ceci et al. 2025) projects, among others.

Appendix B: [Mg V] flux distributions

In Fig. B.1 we present the flux maps for all galaxies with [Mg v]$\lambda5.6098\mu$m emission detected in individual spaxels at a confidence level greater than 5 sigma, along with integrated line profiles considering all spaxels with detected emission. The sample galaxies exhibit diverse flux distributions, ranging from highly collimated structures to more rounded shapes. The discussion on the origin of coronal lines in this sample is beyond the scope of this paper, as we use them solely as a selection criterion. Detailed results on some individual objects, including the analysis of coronal line emission, have already been published on the basis of MIRI MRS data (e.g. Armus et al. 2023; Hermosa Muñoz et al. 2024, 2025; Zhang et al. 2024, Veenema et al, in prep; among others).

Appendix C: W_{80} radial profiles per subsamples

Fig. C.1 presents the W_{80} radial profiles grouping the four emission lines for each subsample, providing a clearer comparison of the differences observed among the distinct emission lines. For the [Mg v] AGN sample (bottom panel) we include also the [Mg v]$\lambda5.6098\mu$m W_{80} values. For the SF sample, the nuclear W_{80} values are typically below 300 km s^{-1}, reaching maximum values of ~450 km s^{-1} farther from the nucleus. The [Ar iii] emission line is detected at radii larger than 1 kpc only for two objects in the SF sample (IRAS 10565+2448 and IRAS 23128-5919), which have higher W_{80} values resulting in the increased values at these distances. For the AGN samples, the lowest W_{80} values are typically observed for H$_2$ and [Ar ii], which show similar values, while the highest values are found for [Fe ii] and [Ar iii]. Among AGN with coronal emission, within the inner ~1 kpc, the highest W_{80} values are observed for [Mg v]. At larger distances, however, the coronal gas shows velocity dispersion similar to that of the other ionized gas lines.

Appendix D: Shock and Photoionization models

Appendix D.1: Shock models

In this work, we use the fast shock models from Pereira-Santaella et al. (2024). These models were computed with the MAPPINGS V code (Dopita & Sutherland 1996; Sutherland & Dopita 2017) and are designed to investigate the origin of ionized gas emission lines in nearby galaxies observed with MIRI/MRS. They follow the prescription of Sutherland & Dopita (2017), varying several parameters: the gas metallicity (Z_{gas}), the shock velocity (v_s), and defining a ram pressure variable as $R_{\mathrm{P}} = \frac{n_{\mathrm{H}}}{\mathrm{cm}^{-3}} \times \left(\frac{v_s}{\mathrm{km/s}}\right)^2$, where n_{H} is the gas volume den-

sity, and the magnetic-to-ram pressure ratio $\eta_{\mathrm{M}} = \frac{B^2}{4\pi\rho v_s^2}$, where B is the magnetic field and ρ the gas density. In this work we adopt models with solar metallicity, shock velocities in the range 80–500 km s^{-1}, and ram pressure parameters $R_{\mathrm{P}} = 10^6$ and 10^8. Further details on the shock models are given in Pereira-Santaella et al. (2024).

Appendix D.2: AGN and SF photoionization models

We used CLOUDY code version c23.01 (Ferland et al. 2017; Chatzikos et al. 2023) to construct grids of photoionization models for AGN and SF, following procedures similar to those described by Pereira-Santaella et al. (2024) and Dors et al. (2012).

For the AGN models, we adopt the ionizing Spectral Energy Distribution (SED) from Jin et al. (2012), based on the OPTXAGNF model (Done et al. 2012). This model describes accretion disk emission with three components powered by a single mass accretion flow: a multicolor blackbody disk producing optical/UV emission, a warm corona generating soft X-rays via Comptonization, and a hot corona responsible for hard X-rays. It is particularly suited for AGN with low Eddington ratios and is included in the CLOUDY SED library.

For the SF models, we generate the SEDs using the STARBURST99 code (Leitherer et al. 1999), adopting an instantaneous SF mode. We assume a Kroupa Initial Mass Function (IMF) (Kroupa 2002), with a slope of $\alpha = 1.3$ for masses between 0.1 and 0.5 M$_\odot$, and $\alpha = 2.3$ for masses from 0.5 to 100 M$_\odot$. We use the Padova evolutionary tracks with solar metallicity (Bressan et al. 1993). The geometry is assumed to be plane-parallel, and the ionization parameter (U) is used to scale the source intensity. We used the SEDs output by the STARBURST99 code for ages ranging from 1 to 10 Myr, in 1 Myr increments, to construct the photoionization models with CLOUDY.

For both AGN and SF models, we adopt solar abundances for all elements based on Grevesse et al. (2010), with an oxygen abundance of $12 + \log(\mathrm{O/H}) = 8.69$. The only exception is iron, which is known to exhibit significant scatter at a fixed O/H value (Izotov et al. 2006). Therefore, we estimate the iron abundance using the relation between iron and oxygen abundances presented by Izotov et al. (2006), resulting in $\log(\mathrm{Fe/H}) \approx -5.60$ for solar oxygen abundance, which is adopted in our models. We adopt grain abundances based on the Orion Nebula, but scale the PAH abundance to match the range observed in local galaxies, as reported by Draine et al. (2007).

We computed a sequence of models with densities spanning $2 \leq \log n_{\mathrm{H}}/\mathrm{cm}^{-3} \leq 6$ and ionization parameters covering $-4.0 \leq \log U \leq -1.0$, both sampled in increments of 1 dex. The models were stopped once the gas temperature fell below 4000 K, the default stopping criterion in CLOUDY. This implies that our models do not predict the H$_2$ emission lines, which are produced at lower temperatures. The stopping criterion is necessary to obtain robust predictions for the ionized gas emission lines, avoiding the complex physics of the transition regions to neutral and molecular gas. Moreover, CLOUDY assumes a simplified one-dimensional structure for AGN, with a central point-like ionizing source and gas in static layers, which is sufficient for modeling the ionized gas emission but does not capture the detailed three-dimensional geometry or the physical conditions in the colder molecular gas regions.

Table A.1. The sample.

Galaxy	RA (HH:MM:SS)	Dec (DD:MM:SS)	Redshift	PID	PI
Arp220	15:34:57.3	23:30:11.4	0.0184	1267	Dicken, D
Centaurus A	13:25:27.6	-43:01:08.8	0.0018	1269	Luetzgendorf, N
Cygnus A	19:59:28.4	40:44:02.1	0.0562	4065	Ogle, P
ESO137-G034	16:35:14.0	-58:04:47.9	0.0095	1670	Shimizu, T
ESO420-G13	04:13:49.7	-32:00:25.2	0.0119	1875	Fernandez Ontiveros, J
IC5063	20:52:02.3	-57:04:07.6	0.0113	2004	Dasyra, K
IIZw96	20:57:24.4	17:07:39.7	0.0361	1328	Armus, L
IRAS05189-2524	05:21:01.4	-25:21:45.4	0.0441	3368	Armus, L
IRAS07251-0248	07:27:37.6	-02:54:54.2	0.0876	3368	Armus, L
IRAS09022-3615	09:04:12.7	-36:27:01.7	0.0596	3368	Armus, L
IRAS09111-1007	09:13:36.5	-10:19:30.1	0.0541	3368	Armus, L
IRAS10565+2448	10:59:18.1	24:32:34.3	0.0431	3368	Armus, L
IRAS-5453	13:15:06.3	-55:09:22.7	0.0308	3368	Armus, L
IRAS14348-1447	14:37:38.4	-15:00:21.3	0.0823	3368	Armus, L
IRAS15250+3608	15:26:59.4	35:58:37.5	0.0552	3368	Armus, L
IRAS19297-0406	19:32:22.3	-04:00:01.0	0.0857	3368	Armus, L
IRAS19542+1110	19:56:35.8	11:19:04.4	0.0650	3368	Armus, L
IRAS20551-4250	20:58:26.8	-42:39:00.3	0.0430	3368	Armus, L
IRAS22491-1808	22:51:49.3	-17:52:24.0	0.0777	3368	Armus, L
IRAS23128-5919	23:15:46.7	-59:03:11.1	0.0446	3368	Armus, L
IRASF01364-1042	01:38:52.8	-10:27:11.8	0.0482	1717	U, V
IRASF08572+3915NW	09:00:25.4	39:03:54.2	0.0582	3869	Veilleux, S
IRASF14378-3651	14:40:59.0	-37:04:31.9	0.0676	3869	Veilleux, S
IRASF23365+3604	23:39:01.3	36:21:08.3	0.0645	3869	Veilleux, S
M81	09:55:33.2	69:03:55.1	-0.0001	2016	Seth, A
M87	12:30:49.4	12:23:28.0	0.0043	2016	Seth, A
M94	12:50:53.1	41:07:13.0	0.0010	2016	Seth, A
M104	12:39:59.4	-11:37:23.0	0.0036	2016	Seth, A
MCG-05-23-016	09:47:40.1	-30:56:56.0	0.0085	1670	Shimizu, T
Mrk231	12:56:14.2	56:52:25.3	0.0422	1268	Maiolino, R
Mrk273	13:44:42.1	55:53:13.5	0.0373	1717	U, V
NGC0253	00:47:33.1	-25:17:18.4	0.0008	1701	Bolatto, A
NGC0424	01:11:27.5	-38:05:01.8	0.0118	6138	Marconcini, C
NGC1052	02:41:04.8	-08:15:20.8	0.0052	2016	Seth, A
NGC1068	02:42:40.8	-00:00:45.9	0.0038	6138	Marconcini, C
NGC1365	03:33:36.5	-36:08:26.7	0.0055	6138	Marconcini, C
NGC1566	04:20:00.2	-54:56:17.2	0.0050	6138	Marconcini, C
NGC1808	05:07:42.4	-37:30:47.0	0.0033	6138	Marconcini, C
NGC3081	09:59:29.5	-22:49:34.8	0.0081	1670	Shimizu, T
NGC3256N	10:27:51.2	-43:54:14.0	0.0094	1328	Armus, L
NGC3256S	10:27:51.2	-43:54:19.2	0.0094	1328	Armus, L
NGC4258	12:18:57.5	47:18:14.3	0.0015	2016	Seth, A
NGC4395	12:25:48.9	33:32:48.7	0.0011	2016	Seth, A
NGC5506	14:13:14.9	-03:12:27.8	0.0061	1670	Shimizu, T
NGC5728	14:42:23.9	-17:15:11.1	0.0092	1670	Shimizu, T
NGC6240	16:52:58.9	02:24:03.7	0.0243	1265	Alonso-Herrero, A
NGC6552	18:00:07.3	66:36:54.3	0.0265	1039	Dicken, D
NGC7172	22:02:01.9	-31:52:10.5	0.0087	1670	Shimizu, T
NGC7319	22:36:03.6	33:58:33.2	0.0225	2732	Pontoppidan, K
NGC7469	23:03:15.6	08:52:26.0	0.0163	1328	Armus, L
NGC7582	23:18:23.6	-42:22:14.1	0.0054	3535	Garcia-Bernete, I
UGC05101	09:35:51.7	61:21:12.3	0.0394	1717	U, V
VV114	01:07:47.5	-17:30:25.2	0.0201	1328	Armus, L
VV340a	14:57:00.7	24:37:02.8	0.0337	1717	U, V

Notes. The galaxy name, coordinates (RA and Dec), redshift, proposal ID (PID), and principal investigator (PI) of the MIRI/MRS proposal are provided, from left to right.
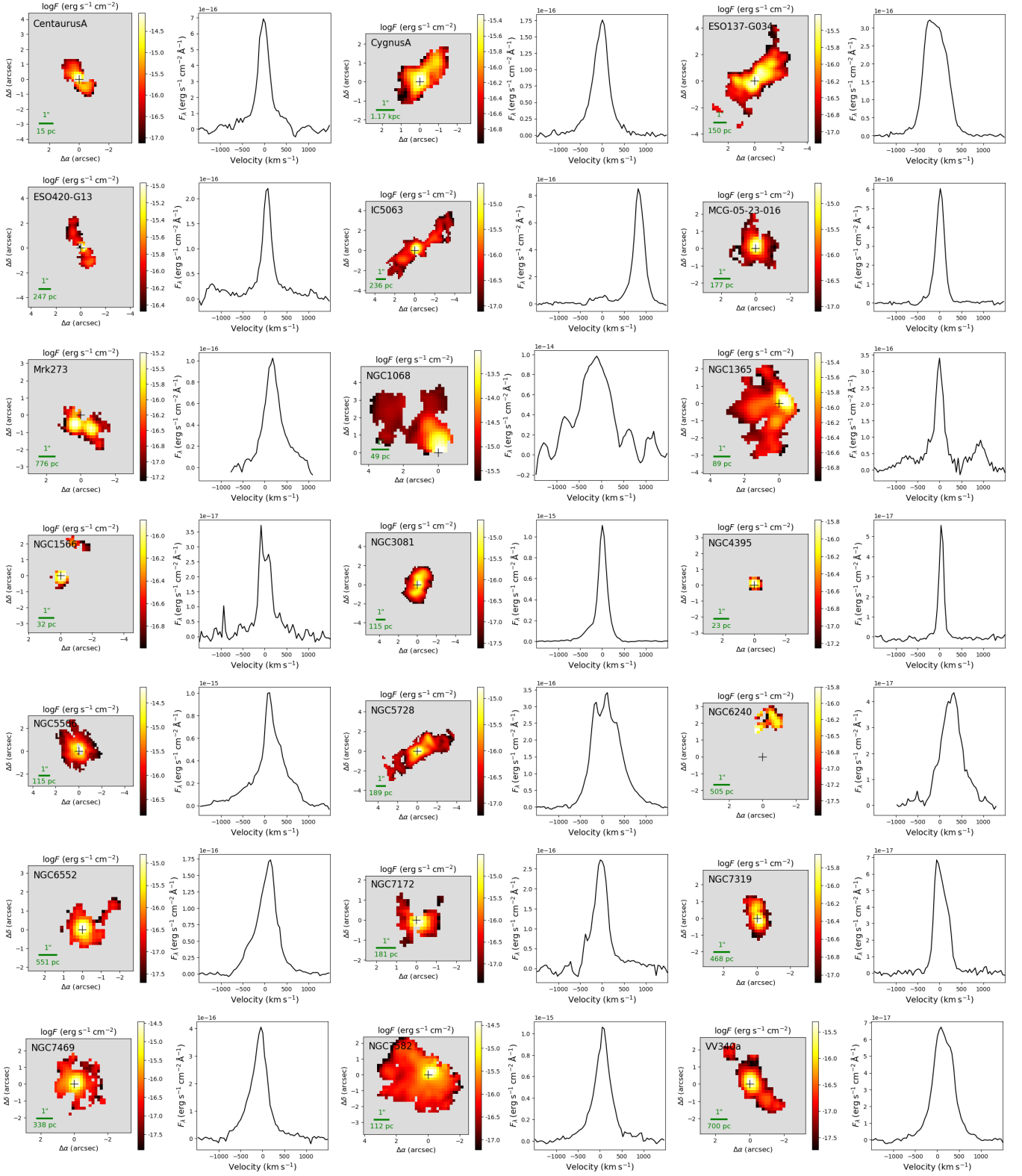
Fig. B.1. [Mg v]$\lambda5.6098\mu$m flux distributions for galaxies with coronal line emission in our sample. The maps illustrate the flux distributions, with gray regions indicating areas where the corresponding emission line is not detected at $SNR > 5$. The plots display the [Mg v]$\lambda5.6098\mu$m integrated profiles, obtained by summing the observed profiles across all detected spaxels and subtracting the continuum. The name of each galaxy is shown in the top-left corner of each plot, the spatial scale is shown in the bottom-left corner, and the central cross marks the position of the galaxy's nucleus.
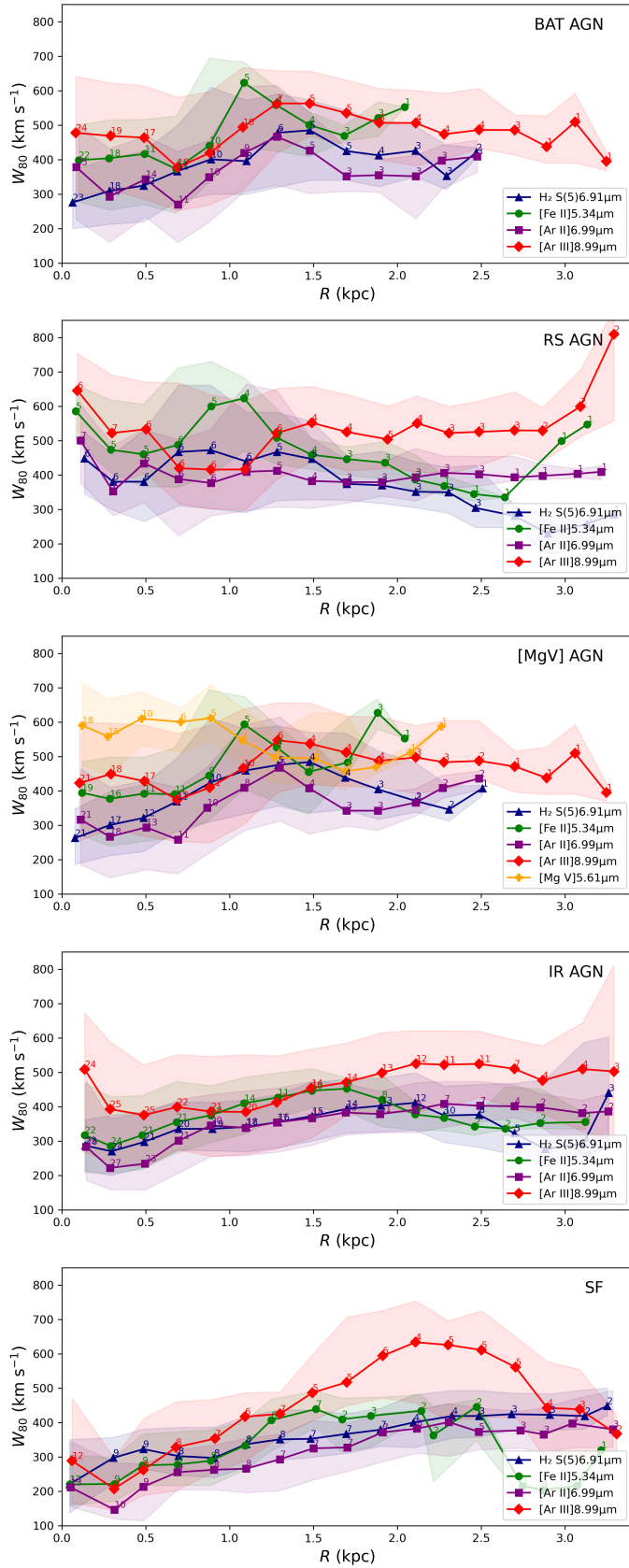
Fig. C.1. The W_{80} radial profiles for the four emission lines are presented for the BAT AGN, RS AGN, [Mg v] AGN, IR AGN and SF subsamples, from top to bottom, respectively. These profiles were computed following the same methodology as those shown in Fig. 5.